

CHIANTI – An atomic database for emission lines. X. Spectral atlas of a cold feature observed with Hinode/EIS

E. Landi¹

and

P. R. Young,^{1,2}

ABSTRACT

In this work we report on a cold, bright portion of an active region observed by EIS. The emitting plasma was very bright at transition region temperatures, and the intensities of lines of ions formed between $10^5 - 10^6$ K were enhanced over normal values. The data set constitutes an excellent laboratory where the emission of transition region ions can be tested. We first determine the thermal structure of the observed plasma, and then we use it 1) to develop a spectral atlas, and 2) to assess the quality of CHIANTI atomic data by comparing predicted emissivities with observed intensities. We identify several lines never observed before in solar spectra, and find an overall excellent agreement between CHIANTI predicted emissivities and observations.

Subject headings: line: identification — atomic data — Sun: corona — Sun: UV radiation — Sun: transition region

1. Introduction

The CHIANTI atomic database (Dere et al. 1997, 2009) provides up-to-date, assessed atomic data for most astrophysically useful ions as well as software for deriving emission line emissivities and synthetic spectra. It has been used to model and interpret emission from a wide range of objects in astrophysics including the Sun's outer atmosphere, the Jupiter-Io plasma torus (Steffl et al. 2008), T Tauri stars (Günther & Schmitt 2008), the interstellar medium (Sallmen et al. 2008) and supernova remnants (Reyes-Iturbide et al. 2008). A vital part of maintaining CHIANTI is the assessment of data quality through comparisons of the

¹Naval Research Laboratory, Space Science Division, Washington, DC 20375

²George Mason University, 4400 University Drive, Fairfax, VA 22030

atomic models with observed spectra. The Sun’s atmosphere is a natural target for such studies as there have been several high resolution spectrometers flown on both rockets and satellites that have produced high signal-to-noise data over large wavelength ranges in the ultraviolet and X-ray regions. In addition, the wide range of structures offered by the Sun – coronal holes, quiet Sun, active regions, flares – yield very different spectra that allow particular atomic models to be studied in different physical conditions. Three previous data assessments have been performed: the comparison of the SERTS-89 rocket flight spectrum with version 1 of CHIANTI by Young et al. (1998); the Landi et al. (2002a,b) comparisons of version 3 of CHIANTI with off-limb quiet Sun spectra obtained with the SUMER and CDS instruments, respectively, on board the SOHO satellite; and the study of an X-ray spectrum obtained with the Flat Crystal Spectrometer on board the Solar Maximum Mission by Landi & Phillips (2006) using version 5 of CHIANTI.

For the present work, an unusual spectrum obtained with the EUV Imaging Spectrometer (EIS, Culhane et al. 2007) on board the Hinode satellite (Kosugi et al. 2007) has been found that shows strongly enhanced lines from the upper transition region corresponding to temperatures $\log(T/K) = 5.0\text{--}5.9$. EIS takes high resolution spectra in the wavelength ranges 170–211 and 246–291 Å and the data represent an excellent opportunity to study atomic physics properties of a group of ions that normally emit weak lines, yet yield valuable information about the emitting plasma.

The paper is structured as follows. First, details of the observation and the procedure for extracting, calibrating, and fitting the spectrum are described. Using lines from all the ions observed by EIS, we determine a first, approximate, differential emission measure (DEM) curve. This is used, together with the L-function method of Landi & Landini (1997), to identify blends or atomic physics issues and select a set of lines free from problems. These are used to determine a more accurate DEM curve. This new curve is used 1) to derive a synthetic spectrum that is used to confirm line identifications in the atlas, and 2) to compare CHIANTI emissivities and observed line intensities for all the ions in the $\log T = 5.0\text{--}5.9$ temperature range that have lines identified in the atlas.

The comparison between CHIANTI emissivities and EIS observations will be split between three separate papers. In the present paper we will consider all elements except iron. In a second paper (Young & Landi 2009) we will discuss the three iron ions Fe VII–IX whose emission is very prominent in the EIS observations we use here, but require special attention due to the large number of lines and of new identifications we made. In a third paper we will carry out the comparison between the CHIANTI emissivities for coronal ions and another set of observations, carried out with a special observing sequence and on a solar target specifically chosen to enhance coronal emission. Thus, we will not consider coronal ions in

the present dataset.

2. Observation

The dataset studied here is the same as that analysed by Young (2009) – a single EIS raster obtained on 2007 February 21 and pointed at active region AR 10942. The complete EIS spectral range is obtained over a $128'' \times 128''$ spatial area with a 25 s exposure at each slit position. Young (2009) selected a spatial area where newly-identified lines of Fe IX were especially strong. For the present work we choose a region of 30 pixels that corresponds to a bright point apparent in Fe VIII images centered at $X=-335''$, $Y=-30''$ (Fig. 1). The bright point appears to be related to the footpoint regions of coronal loops. A SOT magnetogram obtained at 02:00 UT shows that the bright point lies within a unipolar plage region.

The data were calibrated using the standard calibration routine EIS_PREP which is available in the Solarsoft software distribution. EIS_PREP is described in detail by Young et al. (2009), and the routine has been expanded since that work with the following features. Anomalously bright pixels referred to as warm pixels are now directly removed by EIS_PREP through comparison with warm pixel maps obtained by regular engineering studies. For the present observation the warm pixel map was obtained on 2007 March 3. Previously, warm pixels were flagged via the cosmic ray detection algorithm. For full CCD spectra such as those analysed here the method for estimating the CCD background (consisting of the pedestal and dark current) is different to that described by Young et al. (2009). The two 2048×1024 CCDs that measure the two different EIS wavelength bands are each read out as two halves of size 1024×1024 , the four ‘halves’ being referred to as quadrants. For each quadrant an area of 46 pixels wide in the CCD X-direction (corresponding to wavelength) has been identified as being relatively free of emission lines. In each case these areas are where the effective area of the instrument is low. The median value of the data number (DN) values of each pixel in these 46 pixel wide regions are treated as the CCD background for that quadrant, and thus subtracted from the data by EIS_PREP.

As the intrinsic EUV spectrum background is very low in the EIS wavelength bands, a consequence of this method of background subtraction for full CCD data is that a large number of pixels (up to 50 %) can end up with a zero or negative DN value. By default EIS_PREP treats such data points as ‘missing’ data since it is not possible to assign a photon statistics error to them. However, by specifying the keyword /RETAIN the software will assign an error to these points that is simply the estimated dark current error estimate and treat the photon statistics error as zero. This is the option that has been used for the present work.

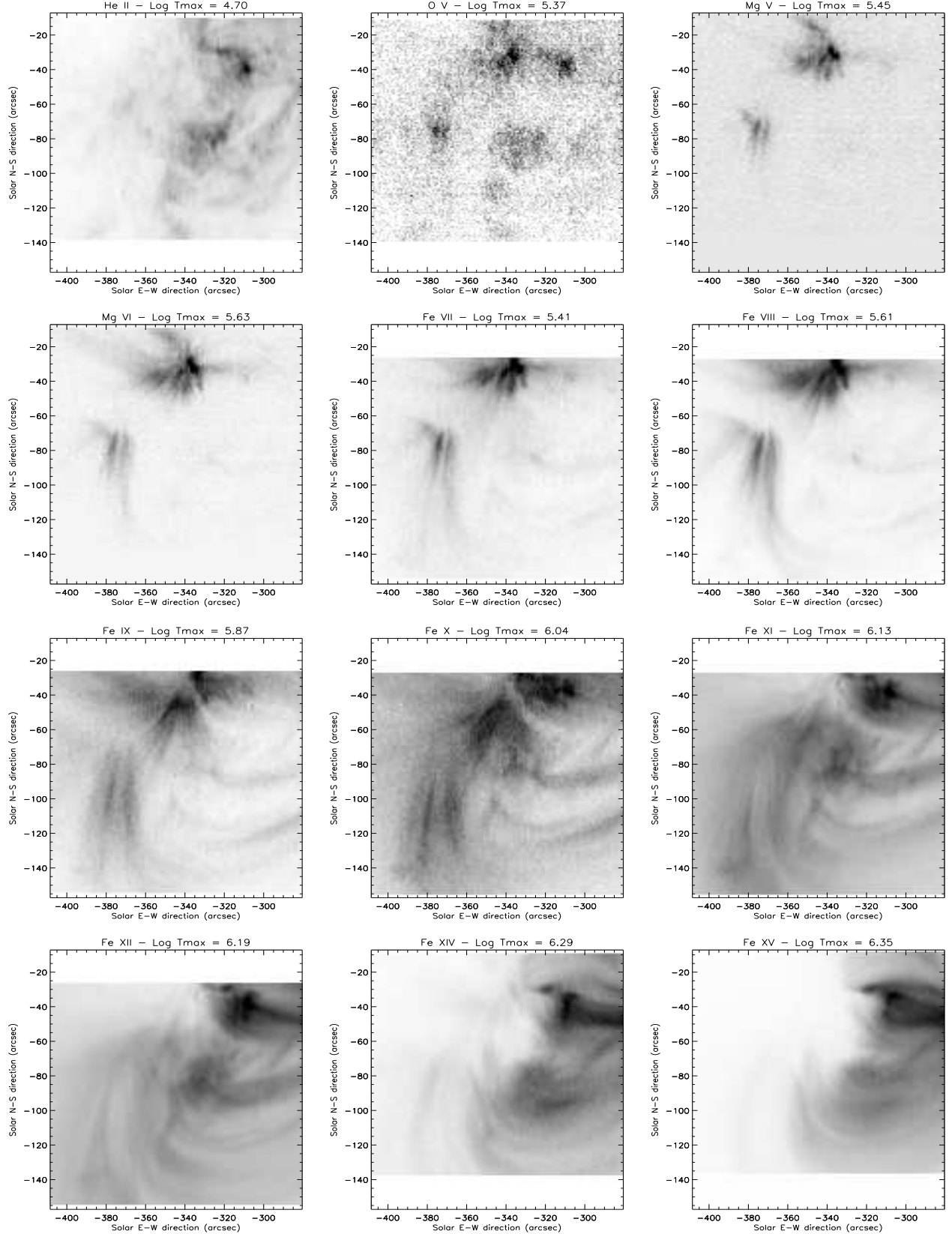


Fig. 1.— Intensity maps for bright lines formed at different temperature regimes. The temperature of maximum abundance, from the CHIANTI 6 ionization equilibrium (Dere *et al.* 2009) is reported as $\log T_{max}$ for each line.

Following the calibration by EIS_PREP, the next step is to average the spectra from the 30 pixel spatial region of interest to yield a single spectrum for analysis. This procedure is complicated by both the CCD spatial offset (Young et al. 2007a) and the EIS spectrum tilt identified by Young et al. (2009), whereby a given spatial feature appears at different CCD Y-positions depending on the wavelength. The routine EIS_CCD_OFFSET in the EIS software tree yields the spatial offset relative to He II $\lambda 256.32$ as a function of wavelength. This routine uses the spectrum tilt gradient derived by Young et al. (2009) for the EIS short wavelength (SW) band and assumes that the same tilt applies to the long wavelength (LW) band. In addition the offset between the SW and LW bands was derived by co-aligning images in Fe VIII $\lambda 185.21$ and Si VII $\lambda 275.35$, which are observed to be very similar to each other. The spatial offsets can be as large as 21 pixels for the shortest and longest wavelength lines observed by EIS.

By specifying a spatial mask in the Fe VIII $\lambda 194.66$ line, the routine EIS_MASK_SPECTRUM takes the level-1 FITS file output by EIS_PREP together with this mask and derives a single spectrum averaged over the specified spatial region. The routine goes through each wavelength in the spectrum and computes an adjusted pixel mask based on the offset relative to $\lambda 194.66$ specified by EIS_CCD_OFFSET. The pixels identified by this adjusted pixel mask are then averaged to yield an intensity value for that wavelength.

The resulting spectrum is calibrated in $\text{erg cm}^{-2} \text{s}^{-1} \text{sr}^{-1} \text{\AA}^{-1}$ units and has an associated error array. The complete spectrum is displayed in Figs. 2–5.

As EIS does not have an internal calibration lamp, it is not possible to derive an absolute wavelength scale for spectra obtained from the instrument without some physical assumption about the observed plasma. The emission line wavelengths given in the present atlas are simply those measured from the spectrum output by EIS_MASK_SPECTRUM and no attempt has been made to adjust them onto a reference scale. Sect. 5 and the individual ion sections of Sect. 6 discuss the velocities derived from particular emission lines. Relative wavelength comparisons for EIS emission lines are estimated to be accurate to a level of $\pm 0.002 \text{\AA}$ (or to within $2.1\text{--}3.5 \text{ km s}^{-1}$, depending on wavelength) based on the work of Brown et al. (2008).

Following creation of a single 1D spectrum for each of the EIS wavelength bands by EIS_MASK_SPECTRUM, the Gaussian fitting routine SPEC_GAUSS_EIS was used to manually derive line fit parameters for each emission line in the spectrum. SPEC_GAUSS_EIS makes use of the MPFIT procedures of C. Markwadt¹. Depending on the density of lines in the spectrum, either lines were fitted individually with single Gaussians, or multiple Gaus-

¹<http://www.physics.wisc.edu/~craigm/idl/>.

sians were fit simultaneously to a group of lines. In cases where good fits were not obtained, it was sometimes necessary to force the widths of the Gaussians to be the same. For two particularly complicated spectral features – the Fe IX–Fe XI–O V blend at 192.5–193.3 Å (Sect. 6.2), and the region around the Si VIII lines at 276–278 Å (Sect. 6.14), a customized fit function was necessary to yield accurate line parameters. The complete list of line fit parameters is given in Table 4.

3. Method of analysis

The present spectrum displays a large number of lines that have either not been identified before or not been studied in any detail. The aim of the present work is thus threefold: (i) to use the lines to determine the density, temperature and DEM of the plasma, (ii) confirm line identifications and check atomic physics properties, and (iii) build the spectral atlas. A variety of techniques are used in the present work and are summarised below.

The most basic method for identifying new lines and line blends is to study an intensity map formed from the line and compare it with a map from an unblended line with a known temperature of formation. The intensity maps that we have taken as a reference are displayed in Figure 1, and the comparison allows us to associate each line to a temperature class. The temperature classes are listed in Table 1, together with the ions most representative of that class, for which we mostly chose iron ions. Note that the temperatures given in Table 1 do not necessarily agree with the temperatures of maximum ionization derived from theoretical calculations (e.g., Bryans et al. 2009) as we believe these calculations are not accurate for some ions. The partition of the ions in so many classes was made possible by the excellent signal-to-noise ratio provided by EIS for some of the lines of each representative ion. In the case of weaker lines, sometimes the small details that discriminate two adjacent classes were lost in the noise: in these cases, both classes are listed in the atlas separated by a dash line: for example, “C-D” means that this line could either belong to class C or to class D.

Intensity map classes also helped us discriminate the cases where lines emitted by ions formed at much different temperatures were blended together. These cases could be easily identified, for example, when intensity maps showed features of both a cold line and a hot line. These cases have been marked by listing in the atlas both classes, separated by a comma: for example “C,L” marks a blend between a C and an L line.

For a number of lines in the atlas it was not possible to assign a temperature class, as the intensity maps were too noisy. For some weak lines the bright knot of emission seen in the cool lines Fig. 1 could be clearly discerned, but it was not possible to clearly assign the

line to a definite class. Such lines are indicated by a spectral class of “A–D” since the knot of emission is a strong feature at each of these temperatures.

Once lines have been identified, or provisionally identified, a first determination of the DEM of the plasma is made using the iterative technique by Landi & Landini (1997). The resulting curve is used in combination with the L-function method by Landi & Landini (1997) to simultaneously compare all the lines from a given ion, yielding density estimates when density sensitive lines are available, and highlighting lines discrepant with theory. The method is described in more detail in Sect. 3.2.

Once a set of emission lines free of blending or atomic data problems has been identified, then these are used to derive a final, more accurate DEM curve. This in turn is used to derive complete CHIANTI synthetic spectra for the EIS wavelength bands, allowing a final check of line blending and identification, and carry out a detailed comparison between CHIANTI emissivities and observed intensities for ions in the $\log T = 5.0$ – 5.9 temperature range.

For calculating line intensities and computing the DEM curve, all atomic data were taken from CHIANTI version 6.0 (Dere et al. 2009). The DEM curve has been derived adopting the ion abundances in Dere et al. (2009) and the Feldman *et al.* (1992) element abundances.

3.1. DEM measurements

The DEM diagnostic technique we use is described in Landi & Landini (1997) and is briefly summarized here. The line flux emitted by an optically thin plasma observed at distance d is given by

$$F_{ij} = \frac{1}{4\pi d^2} \int G(T, N_e) \varphi(T) dT \quad \text{ph cm}^{-2} \text{ s}^{-1} \quad (1)$$

where the Contribution Function is defined as

$$G_{ij}(T, N_e) = \frac{N_j(X^{+m})}{N(X^{+m})} \frac{N(X^{+m})}{N(X)} \frac{N(X)}{N(H)} \frac{N(H)}{N_e} \frac{A_{ij}}{N_e} \quad (2)$$

and the volume Differential Emission Measure (DEM) is defined as

$$\varphi(T) = N_e^2 \frac{dV}{dT} \quad (3)$$

An initial, arbitrary DEM $\varphi_o(T)$ is first adopted; using a correction function $\omega(T)$, the true DEM curve is given by

$$\varphi(T) = \omega(T) \varphi_o(T) \quad (4)$$

If we define the effective temperature T_{eff} as

$$\text{Log}T_{eff} = \frac{\int G_{ij}(T) \varphi(T) \log T dT}{\int G_{ij}(T) \varphi(T) dT} \quad (5)$$

it can be easily shown that, as long as the correction function is slowly varying,

$$I_{ij} = \frac{1}{4\pi} \omega(T_{eff}) \int G_{ij}(T) \varphi_o(T) dT \quad (6)$$

From equation 6, each observed line flux can be used to determine the correction function at temperature T_{eff} ; if lines from many ions are available the $\omega(T)$ curve can be sampled at many temperatures, interpolated, and used to calculate $\varphi(T)$. The resulting $\varphi(T)$ curve is taken as the new trial DEM. Then the procedure is repeated until either the $\omega(T_{eff})$ are all equal to 1 within the errors, or the best χ^2 is reached.

3.2. L-function method of analysis

We used the temperature and density diagnostic procedure that was first introduced by Landi & Landini (1997). This technique relies on the fact that the $G_{ij}(T, N_e)$ curve can be expressed as

$$G_{ij}(T, N_e) = f_{ij}(N_e, T) g(T) \quad (7)$$

where $g(T)$ is the ion abundance, it is function of temperature alone, and it is identical for all the lines of the same ion; while $f_{ij}(N_e, T)$ is the population of the upper level and can be approximated with a linear function of $\log T$ in the temperature range where the line is formed. Landi & Landini (1997) showed that an effective temperature T_{eff} can be defined as

$$\text{Log}T_{eff} = \frac{\int g(T) \varphi(T) \log T dT}{\int g(T) \varphi(T) dT} \quad (8)$$

and used to calculate the effective emission measure $L_{ij}(N_e)$ (L-function) as

$$L_{ij}(N_e) = \frac{I_{obs}}{G_{ij}(T_{eff}, N_e)} \quad (9)$$

If we plot all the L-functions measured for the same ion versus the electron density, all the curves should meet in a common point $(N_e^*, L(N_e^*))$; the L-functions of density independent lines are overlapping and they also cross the same point as the others. An example is shown in Figure 6. Landi & Landini (1997) showed that the abscissa N_e^* of the common point is the density of the emitting plasma.

4. L-function/DEM results

The DEM diagnostic technique described in Sect. 3.1 was applied first to a set of bright emission lines selected from a wide range of ions. The resulting DEM curve is displayed in Figure 7 where it is seen that the emitting region is characterized by a very large and rather broad maximum at around $\log T = 5.7$ that dominates the DEM at all temperatures larger than $\log T = 5.0$. The colder regions of the DEM are similar to the DEM curves available in the literature (and shown in Figure 7, taken from the DEM quiet Sun curve available in the CHIANTI database), but they are much larger. Only in the corona the present DEM shows the same values as the CHIANTI quiet Sun DEM.

With the first-guess DEM defined, the L-functions could be calculated for each line (Sect. 3.2). For each of the ions O IV-VI, Mg VI-VII, Al V,VIII,IX, Si VI-X, S VIII,X, and Fe VIII-XIV more than one emission line is available in the spectrum and so the L-function method was applied to check for discrepancies and identify density diagnostics. A summary of derived densities is given in Table 2. Details of the results of the L-function technique are given in Table 3.

Filtering out emission lines that are clearly discrepant by the L-function method, a new DEM is calculated and the results are shown in Fig. 8. For this DEM we have also added the Fe XV 284.16 Å and Fe XVI 262.98 Å lines to constrain the high temperature part of the DEM curve. Although these latter lines could not be tested using the L-function method as they are the only lines detected from those two ions in the present spectrum, they have been shown in the past to be free of problems (Young *et al.* 1998) and so their use does not introduce any additional uncertainty.

In computing the second DEM curve, a constant density of $\log N_e = 9.15$ was assumed. This value was selected as best value based on the density measurements from each individual

ion listed in Table 2.

The final DEM is quite different from standard solar DEM curves, exhibiting a large maximum at around $\log T = 5.65$ that is responsible for the strongly enhanced lines from the upper transition region ions. A secondary maximum, corresponding to the temperature of the maximum of standard quiet Sun DEMs (also shown in the figure), is located just above $\log T = 6.0$. Some plasma at active region temperatures is also present along the line of sight, but its importance is limited as the DEM curve decreases very rapidly beyond the maximum at $\log T = 6.0$. At nearly all temperatures, the final DEM is larger than the standard quiet Sun DEM from the CHIANTI database.

5. Atlas

The DEM curve shown in Figure 8 was used to calculate a synthetic spectrum that was used to help in the identification of the lines measured in the observed spectrum. Table 4 presents the Gaussian line fit parameters for every emission line in the spectrum, together with line identifications and predicted line intensities for the identified transitions. The coolest ion line in the spectrum is He II Lyman- β , formed at around 80,000 K, and the hottest line is Fe XVI $\lambda 262.98$, formed at around 2.5 million K. Many of the line identifications were given in the spectral atlas of Brown et al. (2008), but some typographical errors in that work have been corrected and, additionally, the DEM analysis has demonstrated that some of the proposed lines of Brown et al. (2008) do not make any significant contribution to the present spectrum. In total there are 277 emission lines listed in Table 4, 103 of which are unidentified.

The EIS dispersion relation was derived by Brown et al. (2007) using mainly strong emission lines from the iron ions Fe IX–XVI and, in particular, none of the cool oxygen, magnesium and silicon species discussed in the following sections were used. Since these lines are very strong in the present spectrum, we can use the measured wavelengths to investigate the accuracy of the reference wavelengths for these ions. Table 6 compares velocities derived using the reference wavelengths given in Table 4 and reference wavelengths given in version 3 of the online NIST Atomic Database. The Table 4 wavelengths are mainly from the work of B. Edlén (Edlén 1979, 1983, 1984, 1985). Individual ions are discussed in Section 6, but we note that the Edlén wavelengths generally give a more consistent set of velocities than the wavelengths obtained from the NIST database. In particular, the strong lines of Mg VII and Si VII which are formed at a very similar temperature, show much better agreement with the Edlén wavelengths.

Table 1: Temperature classes used to classify lines in Table 4.

Class	$\log T$	Ions
A	< 5.45	He II, O IV-VI
B	5.45	Mg V
C	5.60	Fe VII
D	5.75	Fe VIII
E	5.90	Fe IX
F	6.00	Fe X
G	6.05	Fe XI
H	6.20	Fe XII-XIII
I	6.25	Fe XIV
L	6.35	Fe XV
M	6.40	Fe XVI

Table 2: Electron density diagnostics for the selected region. T_{eff} is the effective temperature of the emitting plasma, as defined in Equation 8.

Ion	$\log T_{eff}$ (K)	$\log N_e$ (cm^{-3})
O V	5.50	< 10.5
Mg VI	5.68	> 7.1
Si VII	5.76	> 7.5
Cr VIII	5.77	9.45±0.30
Mg VII	5.78	9.05±0.30
Fe IX	5.81	> 8.8
Fe X	5.92	9.00±0.25
Si VIII	5.90	9.05±0.30
Si IX	5.99	9.20±0.30
Fe XI	6.01	9.35±0.25
Si X	6.08	8.8±0.7
Fe XII	6.09	9.50±0.25
Fe XIII	6.14	9.0±0.2

Comparing the velocities in Table 6 reveals that lines formed between $\log T = 5.2$ to 5.8 generally have a consistent velocity of around $+40 \text{ km s}^{-1}$, while the slightly hotter lines formed between $\log T = 5.8$ to 6.0 are around $+20 \text{ km s}^{-1}$. Inspection of the images in Fig. 1 shows that the bright knot of emission from which the spectrum is obtained is most clearly visible from O V to Fe IX, corresponding to temperatures $\log T = 5.3$ to 5.8 . The change in line velocities is thus likely due to an increasing contamination of the bright point spectrum by other active region emission in the line of sight which is at a different velocity.

6. Individual ion details

In the sections below we discuss identifications and diagnostics, and compare CHIANTI emissivities and observed line intensities for species found in the spectrum. The discussion is focussed towards ions with $\log T_{\text{eff}} \leq 6.0$ as these lines are more intense in this spectrum than other types of solar spectra. For ions outside this temperature range, particularly the iron ions Fe XI–XIV, a detailed study of line ratios and identifications is deferred to a future paper. The results of the L-function diagnostics are given in Table 3, where we provide the L-function values of all the lines and their ratios to the lowest one, calculated at the crossing point. If all lines are density insensitive relative to each other, or the L-functions do not provide a clear indication of $\log N_e$, the ratios were calculated assuming $\log N_e = 9.15$. Each line intensity has been associated to an uncertainty of 20%, to account for atomic data uncertainties.

Table 3. L-function results.

λ	$L(T_{eff})$	Ratio	Notes
O IV	$\log T_{eff} = 5.19$		
279.67	15.09 ± 0.09	0.69	NO
279.97	15.25 ± 0.09	1.00	OK
260.30	15.27 ± 0.09	1.04	OK
O V	$\log T_{eff} = 5.50$		
185.78	15.55 ± 0.12	3.31	Unidentified blend; O V \simeq 30%
192.81	15.46 ± 0.09	6.99	Blended with Fe XI; O V \simeq 37%
192.93	15.03 ± 0.09	1.00	Blended with Fe XI; O V \simeq 100% – OK
248.49	15.11 ± 0.09	1.20	Blended with Al VIII; O V \simeq 83% – OK
271.07	15.40 ± 0.09	2.34	Blended with Fe VII; O V \simeq 43%
O VI	$\log T_{eff} = 5.65$		
172.93	$16.09^{+0.19}_{-0.34}$	1.74	OK
173.12	$15.97^{+0.15}_{-0.24}$	1.32	OK
183.95	15.98 ± 0.09	1.35	Unidentified blend; O VI \simeq 74%
184.14	15.85 ± 0.09	1.00	OK
Mg VI	$\log T_{eff} = 5.66$		
269.02	15.76 ± 0.09	1.00	OK
270.43	15.80 ± 0.09	1.10	OK
Mg VII	$\log T_{eff} = 5.76$		
276.17	15.73 ± 0.09	1.00	OK
277.04	15.73 ± 0.09	1.00	OK
278.44	15.75 ± 0.09	1.05	OK
280.76	15.77 ± 0.09	1.10	OK
Al V	$\log T_{eff} = 5.56$		
278.73	15.74 ± 0.09	1.35	Ni XI; Al V \simeq 74% – OK
281.44	15.61 ± 0.09	1.00	OK

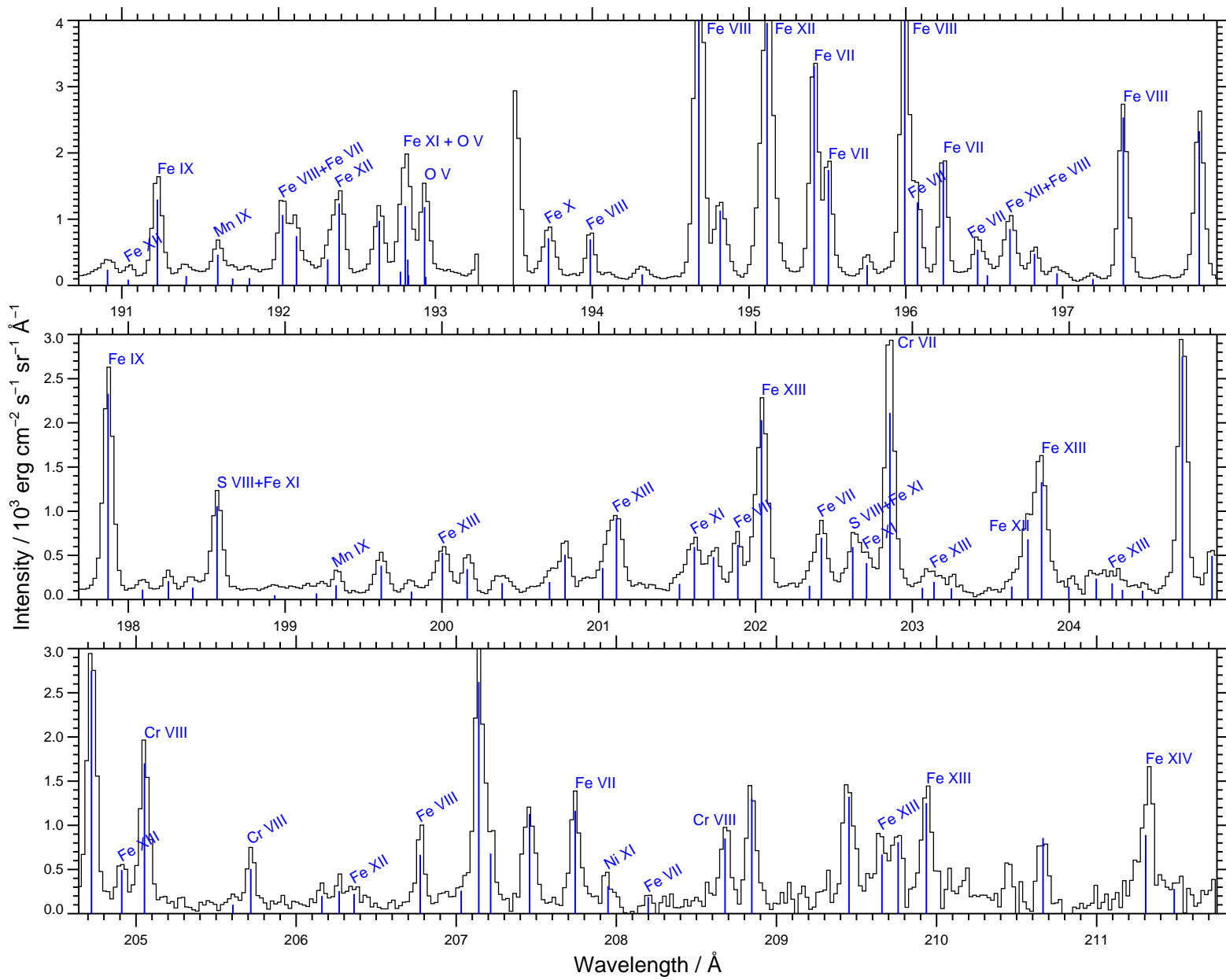


Fig. 3.— Panels showing the second half of the EIS SW spectrum. See the caption of Fig. 2 for more details. Note the gap around 193.4 \AA which is due to dust on the EIS detector blocking the spectral signal. The long wavelength half of the Fe XII λ 193.51 line profile can be seen at 193.5 \AA .

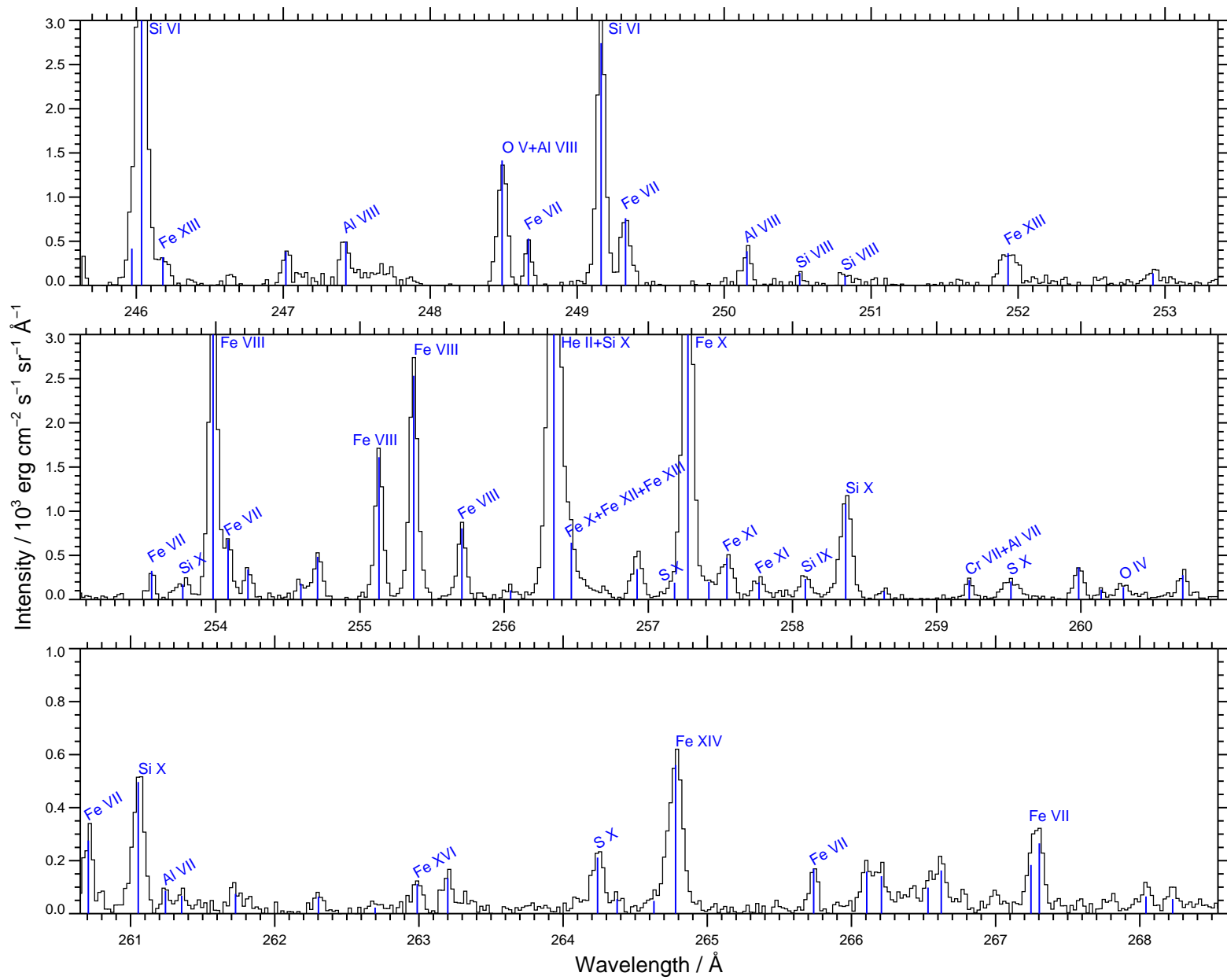


Fig. 4.— Panels showing the short wavelength half of the EIS LW spectrum. See the caption of Fig. 2 for more details.

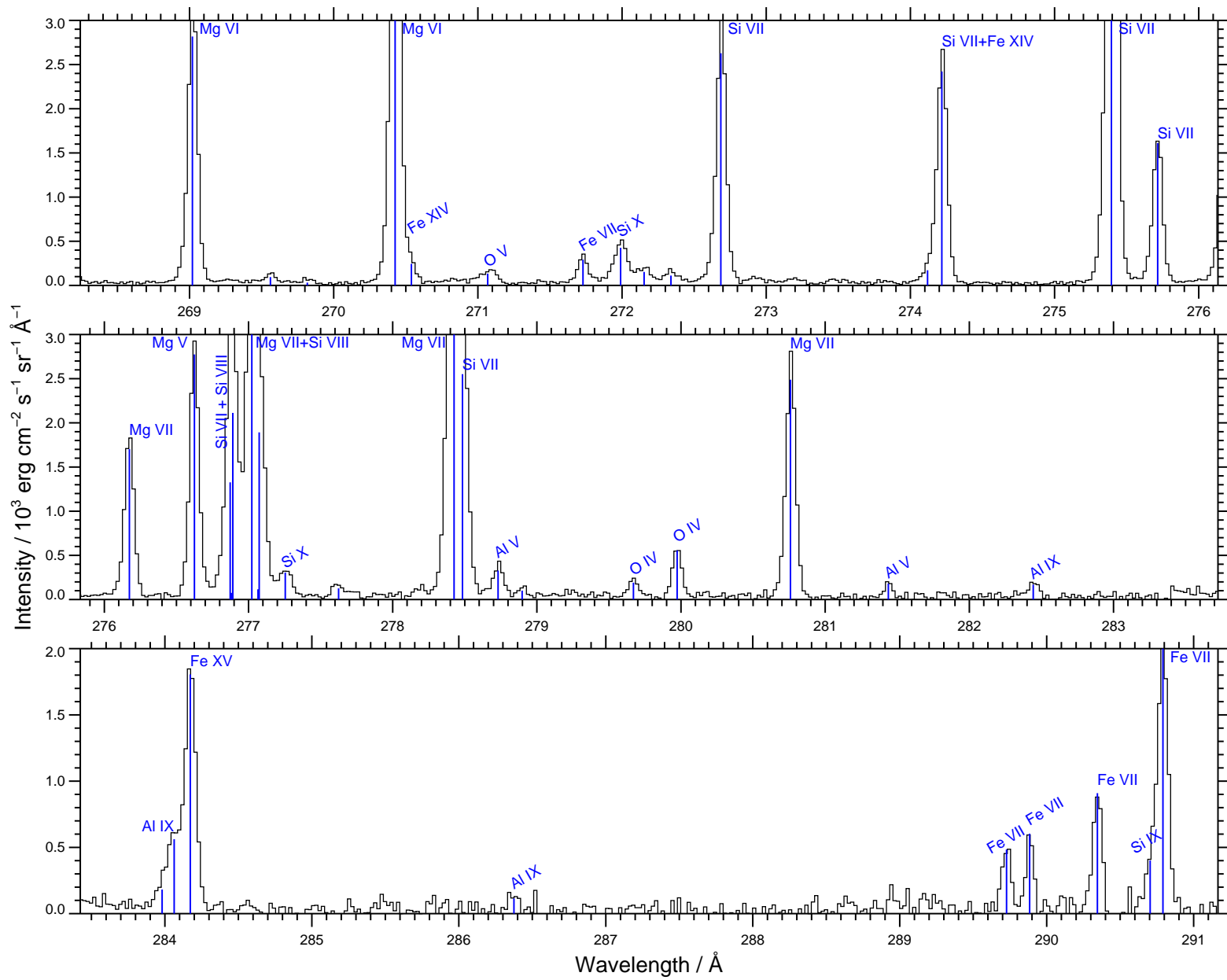


Fig. 5.— Panels showing the long wavelength half of the EIS LW spectrum. See the caption of Fig. 2 for more details.

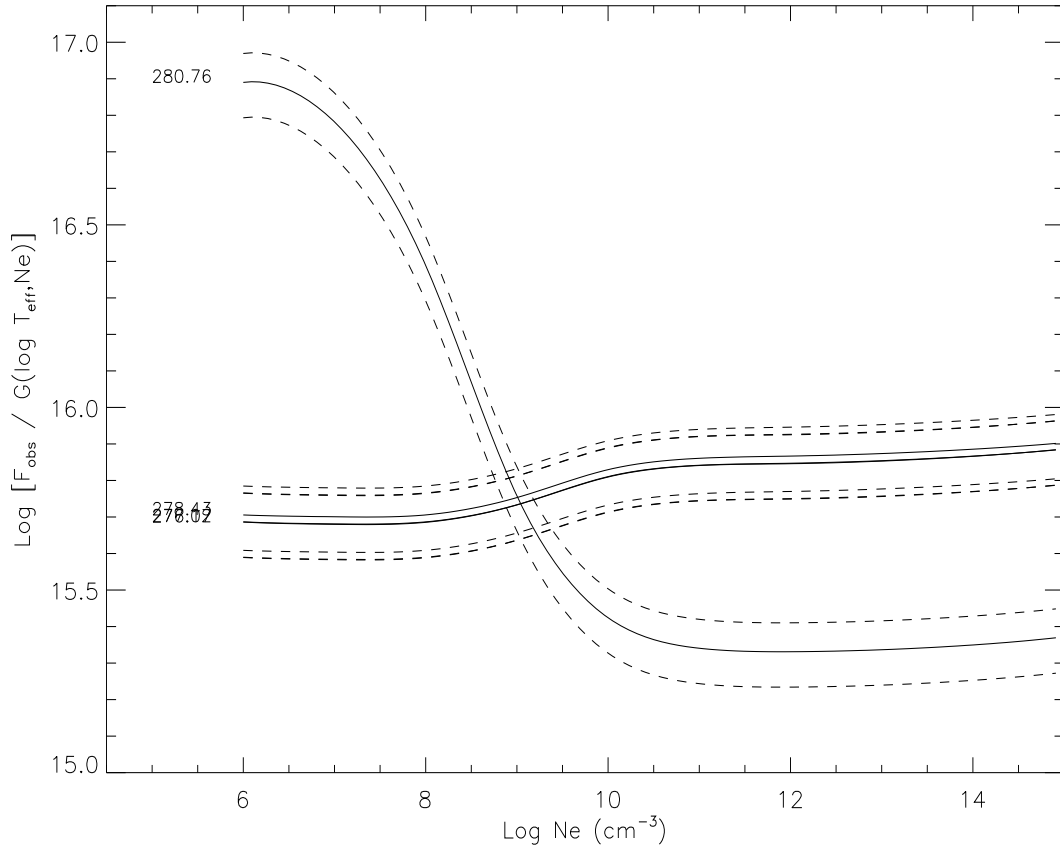


Fig. 6.— L-function curves of the Mg VII lines, with a 20% uncertainty (dotted lines). Two Mg VII lines provide coincident L-functions.

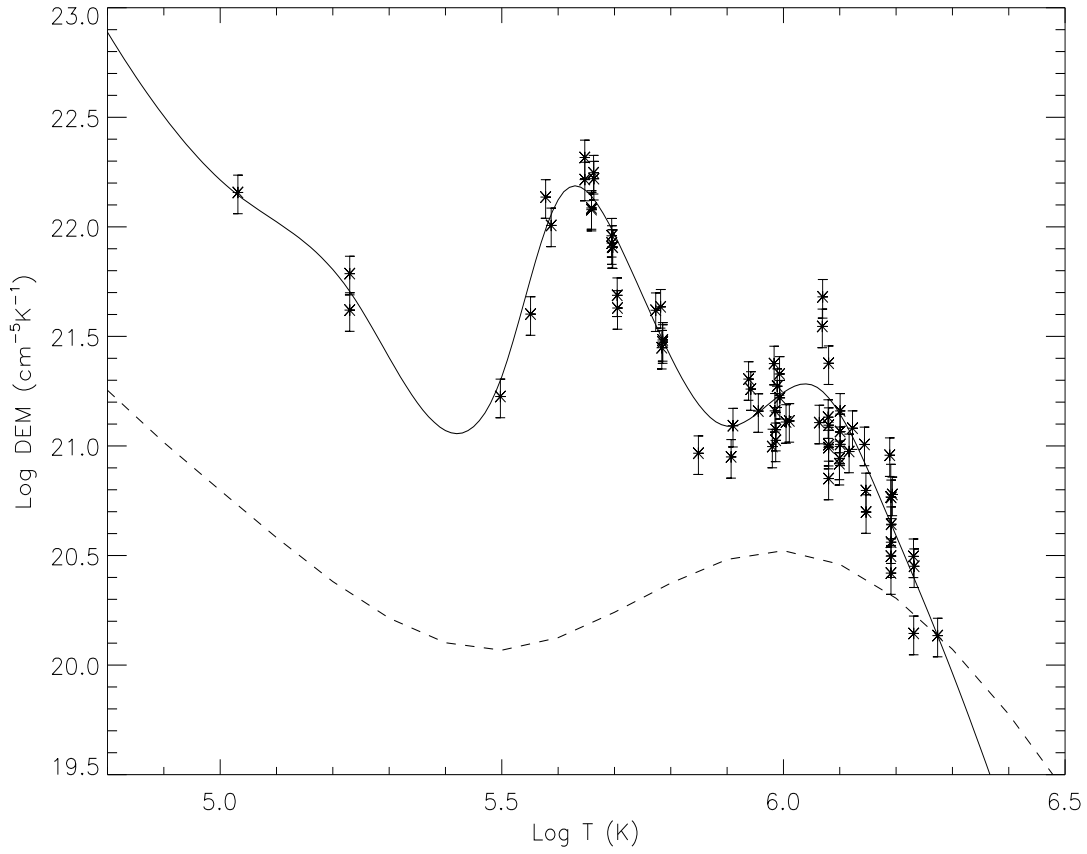


Fig. 7.— DEM curve obtained before using the L-function method. The CHIANTI quiet Sun DEM is superimposed for comparison purposes.

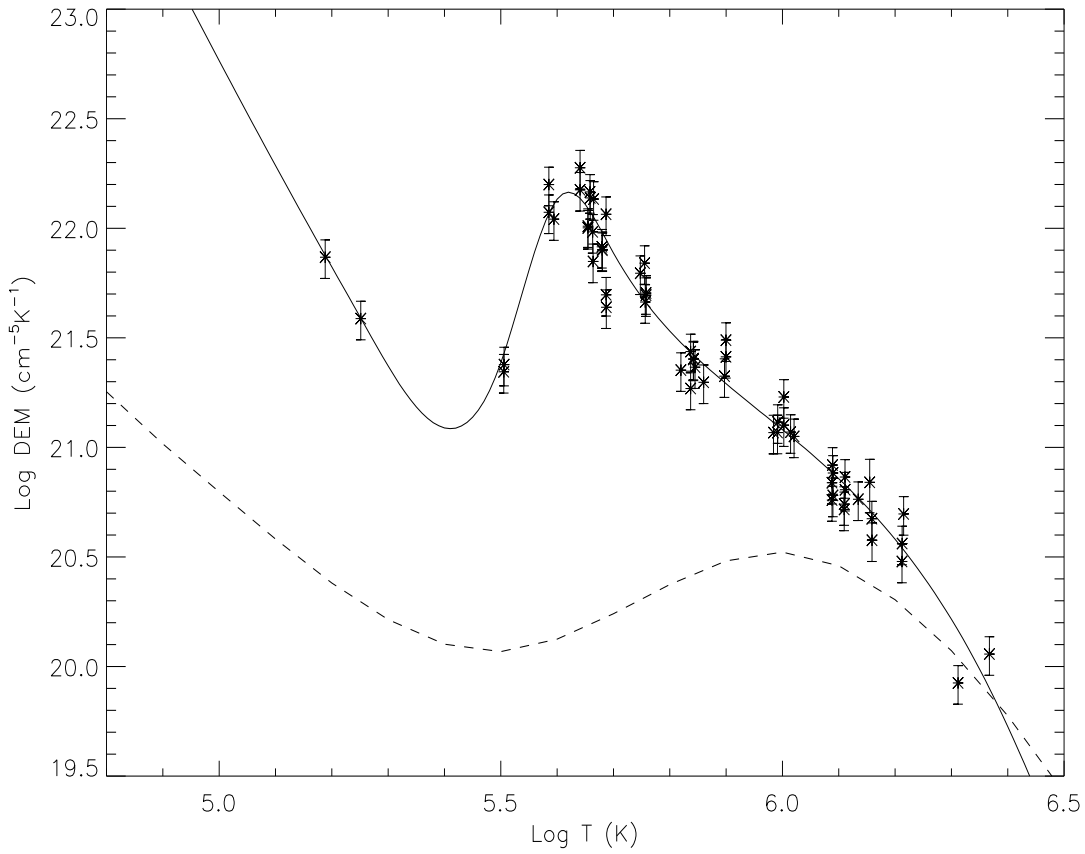


Fig. 8.— DEM curve obtained with the spectral lines selected using the L-function method. The CHIANTI quiet Sun DEM is superimposed for comparison purposes. The lines used for generating this DEM curve had been previously selected with the L-function method and the first-cut DEM curve in Figure 7.

Table 3—Continued

λ	$L(T_{eff})$	Ratio	Notes
<hr/>			
Al VII	$\log T_{eff} = 5.76$		
259.23	16.33 ± 0.09	5.89	Blend Cr VII; Al VII \simeq 17% – NO
261.24	15.56 ± 0.09	1.00	OK
<hr/>			
Al VIII	$\log T_{eff} = 5.90$		
247.43	16.20 ± 0.09	6.61	Unidentified blend; Al VIII \simeq 15%
248.49	16.23 ± 0.09	7.08	Blended with O V; Al VIII \simeq 15% – OK
250.16	15.38 ± 0.09	1.00	OK
<hr/>			
Al IX	$\log T_{eff} = 6.00$		
282.44	15.31 ± 0.09	1.35	Unidentified blend; Al IX \simeq 74%
284.06	15.42 ± 0.09	1.74	Unidentified blend; Al IX \simeq 58%
286.38	15.18 ± 0.09	1.00	
<hr/>			
Si VI	$\log T_{eff} = 5.66$		
246.04	15.64 ± 0.09	1.02	OK
249.16	15.63 ± 0.09	1.00	OK
<hr/>			
Si VII	$\log T_{eff} = 5.76$		
272.69	15.64 ± 0.09	1.10	OK
274.22	15.79 ± 0.09	1.55	Blend Fe XIV; Si VII \simeq 65%
275.39	15.60 ± 0.09	1.00	OK
275.71	15.64 ± 0.09	1.10	OK
276.88	15.64 ± 0.09	1.10	OK
278.44	15.62 ± 0.09	1.05	OK
<hr/>			
Si VIII	$\log T_{eff} = 5.90$		
250.51	15.70 ± 0.09	1.23	OK
250.82	15.62 ± 0.09	1.02	OK
276.85	15.63 ± 0.09	1.05	OK
276.87	15.61 ± 0.09	1.00	OK

Table 3—Continued

λ	$L(T_{eff})$	Ratio	Notes
277.04	15.63 ± 0.09	1.05	OK
277.06	15.61 ± 0.09	1.00	OK
<hr/>			
Si IX	$\log T_{eff} = 6.02$		
258.09	15.20 ± 0.09	1.05	OK
290.71	15.18 ± 0.09	1.00	OK
<hr/>			
S VIII	$\log T_{eff} = 5.88$		
198.57	15.75 ± 0.09	1.00	Blend Fe XI
202.62	15.88 ± 0.09	1.35	Blend Fe XI
<hr/>			
Cr VII	$\log T_{eff} = 5.66$		
202.86	15.66 ± 0.09	1.00	OK
258.64	16.27 ± 0.09	4.07	Unidentified blend; Cr VII \simeq 25%
259.23	16.33 ± 0.09	4.67	Blend Al VII; Cr VII \simeq 21% – NO
261.35	16.68 ± 0.09	10.50	Unidentified blend; Cr VII \simeq 10%
<hr/>			
Cr VIII	$\log T_{eff} = 5.77$		
205.05	16.06 ± 0.09	1.00	OK
205.72	16.09 ± 0.09	1.07	OK
208.68	16.11 ± 0.09	1.12	OK
211.48	16.08 ± 0.09	1.05	Blend Ni XI; Cr VIII \simeq 95% – NO
<hr/>			
Mn VIII	$\log T_{eff} = 5.71$		
185.46	15.73 ± 0.09	1.00	OK
263.20	16.10 ± 0.09	2.34	Unidentified blend; Mn VIII \simeq 43%
<hr/>			
Mn IX	$\log T_{eff} = 5.86$		
188.43	15.97 ± 0.09	1.59	Blend Fe VII
191.61	16.00 ± 0.09	1.70	
199.33	15.77 ± 0.09	1.00	

In Table 3, if a ratio is less than 1 it indicates the measured line intensity is weaker than predicted by theory, while a ratio greater than 1 indicates the measured line is stronger than predicted by theory. Usually the latter case is due to a blending line.

6.1. O IV

A large number of $n = 2$ to $n = 3$ transitions lie in the wavelength range 170–292 Å, with the brightest two lines falling between the two EIS wavebands at around 238.5 Å. The next strongest is the $2s^22p\ ^2P_{3/2} - 2s^23s\ ^2S_{1/2}$ transition at 279.933 Å, which is seen in the EIS spectrum. Another decay from this upper level to $2s^22p\ ^2P_{1/2}$ falls nearby at 279.631 Å and this is also seen in the spectrum. While the observed separation of the two lines is in excellent agreement with the wavelengths of Edlén (1934), the branching ratio of the lines shows a significant discrepancy with the prediction from CHIANTI: the predicted ratio being 0.50 compared to the observed ratio of 0.34 ± 0.05 . The line widths show no indication of blends (Table 4), and the L-function method suggests the $\lambda 279.93$ yields the best agreement between theory and observation (Tables 3 and 4).

A number of transitions between excited configurations are predicted in the EIS wavelength range, the strongest of which is potentially observable. The $2s2p^2\ ^2D_{5/2} - 2s2p(^3P)3d\ ^2F_{7/2}$ transition was found at 260.389 Å by Edlén (1934). A possible candidate is the line measured at 260.292 Å for which the intensity is in excellent agreement with $\lambda 279.93$ (Table 3), however the wavelength shows a significant discrepancy: the measured wavelength implying a velocity of -112 km s^{-1} compared to $+43\text{ km s}^{-1}$ for $\lambda 279.93$. The width of the line is also significantly broader than $\lambda 279.93$. The ratios of the observed 260.29 Å line relative to either $\lambda 279.63$ or $\lambda 279.93$ are excellent temperature diagnostics with little sensitivity to density and the derived values are $\log T = 5.18 \pm 0.05$ and 5.30 ± 0.07 for $\lambda 279.93$

Table 3—Continued

λ	$L(T_{eff})$	Ratio	Notes
Ni XI $\log T_{eff} = 5.95$			
207.95	15.26 ± 0.09	1.00	OK
211.48	15.51 ± 0.09	1.78	Blend Cr VIII; Ni XI $\simeq 56\%$ – NO
278.73	16.17 ± 0.09	8.13	Blend Al V; Ni XI $\simeq 12\%$ – OK

and $\lambda 279.63$, respectively.

Additional weak lines are expected to fall in the EIS wave bands, but they are less intense than those reported in the atlas, and they are not found in the spectrum. A line with rest wavelength 203.044 \AA is a good wavelength match for the line observed at 203.064 \AA but the observed intensity is a factor 5 larger than predicted, so O IV only provides a minor contribution to the observed feature.

6.2. O V

There are several O V lines in the EIS wavelength range, but most are affected by blending. A few of these lines are density sensitive relative to each other, but they only allow to determine an upper limit to the plasma electron density, $\log N_e < 10.5$. The strongest line by intensity is the $2s2p \ ^1P_1 - 2s3s \ ^1S_0$ transition at 248.46 \AA , which is blended with an Al VIII line. Table 3 shows that the contribution of Al VIII to the line is $\simeq 15\%$ in agreement with the L-function results for Al VIII.

A group of six transitions from the $2s2p \ ^3P - 2s3d \ ^3D$ multiplet are found between 192.75 and 192.91 \AA and have been discussed by Young et al. (2007b). They are partly blended with Fe XI and Ca XVII lines and a method to extract the intensities of the individual component lines has been described by Ko et al. (2009). In the present case a slightly modified treatment is used since there is very little high temperature emission in the spectrum and so Ca XVII can be safely ignored. In addition a nearby line at 192.64 \AA , which we believe is due to Fe IX (Young & Landi 2009) is quite strong and needs to be accounted for in the fit. We include six Gaussians for the six O V lines, with the separations being fixed to the separations of the CHIANTI wavelengths and the widths forced to be the same. Although there is some density sensitivity amongst the lines, it is small and we force the lines to have the relative strengths predicted by CHIANTI at a density of 10^{10} cm^{-3} . In summary, then, the only free parameters for the O V lines are taken to be the wavelength, width and amplitude of the $\lambda 192.904$ line (the strongest of the group), with the parameters for the other lines all fixed relative to this. For Fe XI $\lambda 192.83$ and the line at 192.64 \AA we fit two independent Gaussians. Note that the additional Fe XI $\lambda 192.90$ line discussed by Ko et al. (2009) is not included as it is very weak. The resulting fit parameters for the Gaussians are given in Table 4. Note that the fit parameters for each of the O V lines except $\lambda 192.904$ are derived from the $\lambda 192.904$ fit parameters as described above. Confidence in the derived fit parameters is obtained by comparing the velocity shifts of $\lambda 192.83$ and $\lambda 192.904$ (-36 km s^{-1} and $+42 \text{ km s}^{-1}$, respectively) with Fe XI $\lambda 188.23$ and O V $\lambda 248.46$ (-35 km s^{-1} and $+35 \text{ km s}^{-1}$, respectively).

Three further O v lines are predicted in the EIS wavebands. $\lambda 172.17$ is comparable in strength to $\lambda 192.90$ but the instrument effective area is much lower in this part of the spectrum. A couple of lines are indeed barely visible at around $\lambda 172.0$ – 172.3 but they are too weak to provide a reliable measurement of their parameters. The observed line at 185.780 \AA is a good wavelength match for O v $\lambda 185.745$ however the intensity map for the line indicates that it is emitted by an unidentified hotter ion formed at temperatures closer to Mg v and Fe VII. Indeed, Table 3 indicates that O v provides only $\simeq 30\%$ of the observed intensity. The other O v line identified in the long wavelength section of the atlas is $\lambda 271.068$, which sits in a rather broad spectral feature to which Fe VII $\lambda 271.074$ also contributes (Young & Landi 2009). We estimate O v accounts for $\simeq 43\%$ of the measured intensity.

6.3. O VI

The $2p^2 P_{1/2,3/2} - 3s^2 S_{1/2}$ transitions, $\lambda\lambda 183.94, 184.12$, are seen in the present spectrum and their intensities are reproduced reasonably well by the DEM (Table 4). However their L-functions show a small, but significant, discrepancy with theory (Table 3), with $\lambda 183.94$ observed to be too strong compared to $\lambda 184.12$ by a factor 1.35. This is surprising for such a simple ion and the obvious solution is that $\lambda 183.94$ is blended. However, images formed in both lines are very similar and show no evidence of a contribution from a line formed at a different temperature. In terms of line widths, $\lambda 183.94$ is actually found to be a little narrower than $\lambda 184.12$ and so any blending line must lie at almost exactly the same wavelength as $\lambda 183.94$. Comparing the measured wavelengths with the rest wavelengths of Edlén (1979) and converting to velocity units gives $+19.6 \pm 3.3$ and $+35.8 \pm 3.3 \text{ km s}^{-1}$ for $\lambda 183.94$ and $\lambda 184.12$, respectively. The separation of the lines is thus not consistent with their rest wavelengths. The velocity of $\lambda 184.12$ is more consistent with other ions formed at a similar temperature (Table 6), suggesting problems with the $\lambda 183.94$ line. A study of $\lambda 183.94$ and $\lambda 184.12$ in a range of different conditions would be valuable for further investigating these problems.

The only other O VI lines expected in the EIS spectrum are the three transitions of the $2p^2 P_J - 3d^2 D_J$ multiplet. The strongest line ($3/2$ – $5/2$) has a rest wavelength of 173.080 \AA and is partly blended with the $3/2$ – $3/2$ transition at 173.095 \AA although the latter is predicted to be a factor 0.17 smaller. The $1/2$ – $3/2$ transition is at 172.936 \AA . The EIS effective area is very low at these wavelengths, but two lines can be seen close to these wavelengths (Table 4). Converting the measured wavelengths to velocity units gives -17 ± 25 and $69 \pm 29 \text{ km s}^{-1}$ for $\lambda 172.94$ and $\lambda 173.08$, respectively, and so only the latter line is consistent with the velocities of $\lambda 183.94$ and $\lambda 184.12$ presented above. The intensities of these lines are a little larger

than expected relative to the $\lambda 184.14$ (Table 3), but the uncertainties are larger than the difference.

6.4. Ne v

A number of weak Ne v transitions are predicted through the EIS wavebands and the strongest in terms of counts expected on the detector is $\lambda 184.735$ which is a possible wavelength match for an observed line at 184.777 \AA although the implied velocity of $+68 \text{ km s}^{-1}$ is larger than found for O v (Table 6) which is formed at a similar temperature. The intensity predicted from the DEM shows that the Ne v line cannot fully account for the 184.777 \AA line’s intensity and other contributions come from Fe VII and Fe XI (Table 4). A Ne v line at 173.932 \AA is predicted to be stronger than $\lambda 184.735$ by a factor three, but the EIS sensitivity is low at this wavelength and the line can not be seen. No trace is found of the other Ne v lines predicted by CHIANTI, with the only exception of $\lambda 274.090$, which lies close to an observed and unidentified line at 274.119 \AA , whose intensity image is consistent with a cool line. However, we hesitate to identify this line as Ne v since the predicted intensity is factor 4 lower than observed, and other Ne v lines predicted to be brighter are not observed.

6.5. Ne vi

The only Ne vi lines predicted to be observable in the EIS wavelength range belong to the $2s2p^2 \text{ } ^2\text{S}_{1/2} - 2s^22p \text{ } ^2\text{P}_{1/2,3/2}$ doublet at 185.056 and 184.945 \AA , respectively. The strongest of the two lines is close to the observed line at 184.922 \AA , however the velocity of -37 km s^{-1} is discrepant with the O vi $\lambda 184.12$ velocity of $+39 \text{ km s}^{-1}$. The intensity prediction from the DEM analysis (Table 4) shows that Ne vi can only account for $\simeq 50\%$ of the observed intensity, and the remaining contribution is due to Fe VII $\lambda 184.886$. The Ne vi $\lambda 185.056$ line is predicted to be around half the strength of $\lambda 184.945$, but it is not found in the spectrum.

6.6. Mg v

Mg v provides one strong line in the EIS spectrum, given by the allowed $2s^22p^4 \text{ } ^1\text{D} - 2s2p^5 \text{ } ^1\text{P}$ transition observed at 276.625 \AA . This line is very prominent in the present dataset, as Mg v is formed at temperatures close to the peak temperature of the DEM curve and the intensity predicted from the DEM is very close to the measured intensity (Table 4).

Using the rest wavelength of Edlén (1983) gives a velocity of $49.9 \pm 0.05 \text{ km s}^{-1}$ which is around 10 km s^{-1} larger than the average velocity of the lines formed below $\log T = 5.8$, suggesting the rest wavelength may be slightly in error. No other Mg v line is identified in the atlas, because the few other lines available in the EIS range are much weaker than $\lambda 276.625$. Only two lines are potentially observable: they are weak, but are predicted to be at $\simeq 197 \text{ \AA}$, where the EIS coating reflectivity is high. However, their wavelengths are based on calculated rather than laboratory level energies, so that it is difficult to associate them with any spectral line with certainty. Table 1 lists Mg v as class B, but the few unidentified lines listed as class B or even C are brighter by an order of magnitude than the predicted Mg v lines.

6.7. Mg VI

The $2s^2 2p^3 \ ^2D_J - 2s 2p^4 \ ^2P_{J'}$ multiplet gives rise to two strong lines in the present spectrum: the $3/2-1/2$ transition at 269.020 \AA and the $5/2-3/2$ transition at 270.426 \AA . The latter is blended with the $3/2-3/2$ component which is predicted by CHIANTI to be 13 % of the $5/2-3/2$ component, and the fitted Gaussian at 270.426 \AA includes both components. A further blend is with Fe XIV $\lambda 270.52$ which normally dominates in active region conditions. In the present spectrum, however, the Fe XIV component is weak and can be fit with a separate Gaussian. Table 3 demonstrates that the two observed lines are in good agreement with each other, however the DEM over-predicts the strength of both lines by around 20 % (Table 4). Table 6 shows that the velocities derived using the reference wavelengths of Edlén (1984) are consistent with the other cool species in the spectrum. Note that the slightly larger velocity for the 270.426 \AA line is likely due to the weaker blending line which has a slightly longer rest wavelength.

The CHIANTI Mg VI model predicts many $n = 2$ to $n = 3$ transitions in the EIS wavebands, but all are very weak and can not be observed in the present spectrum.

6.8. Mg VII

Only four lines of significant strength are expected in the EIS wavebands, and each is bright in the current spectrum. The three members of the $2s^2 2p^2 \ ^3P_J - 2s 2p^3 \ ^3S_1$ multiplet are expected at 276.14 , 276.99 and 278.39 \AA , but only the weakest line, $\lambda 276.14$, is unblended. $\lambda 276.99$ is blended with Si VIII and a method for extracting the line intensities in this difficult part of the spectrum is described in Sect. 6.15. Although $\lambda 276.99$ is listed in Table 4 we note

that the parameters were completely determined from the $\lambda 276.14$ parameters and so this is not an independent measurement. $\lambda 278.39$ is blended with Si VII $\lambda 278.45$ but by fitting two Gaussians forced to have the same width, the two lines' intensities can be extracted. The $2s^2 2p^2 \ ^1D_2 - 2s 2p^3 \ ^1P_1$ transition is found at 280.72 \AA , and forms an excellent density diagnostic with any of the $2s^2 2p^2 \ ^3P_J - 2s 2p^3 \ ^3S_1$ multiplet.

Table 3 shows that $\lambda 276.14$, $\lambda 278.39$ and $\lambda 280.72$ are in good agreement with each other, however the DEM underpredicts the lines' intensities by around 40 %. Using the reference wavelengths of Edlén (1985) yields velocities for $\lambda 276.14$, $\lambda 278.39$ and $\lambda 280.72$ that are in good agreement with the other ion species formed below $\log T = 5.8$. However, we note that using the reference wavelengths from the NIST database gives significantly lower velocities. The best agreement among Mg VII lines is found at $\log N_e = 9.05 \pm 0.30$.

6.9. Al V

The $2s^2 2p^5 \ ^2P_{3/2,1/2} - 2s 2p^6 \ ^2S_{1/2}$ transitions at 278.69 and 281.39 \AA , respectively, are the only Al V lines visible in the EIS wavelength band. They are emitted by the same upper level so they can not be used for temperature or density diagnostics. These two lines disagree with each other, because the 278.73 line is affected by a relatively weak blend due to a previously unidentified Ni XI line, expected to account for $\simeq 25\%$ of the observed intensity. The predicted Ni XI line intensity is a bit lower than needed, but the combined intensity of the two lines is reasonably close to the observed value. The $\lambda 281.438$ line is very close to a S XI feature prominent in active region plasmas, but in the present dataset the contribution of this line is negligible.

The velocities of the two Al V lines are consistent with other species (Table 6) when using the reference wavelengths of Artru & Brillet (1974), and the DEM predictions for the two lines are in good agreement with measurements.

6.10. Al VII

Four transitions of the $2s^2 2p^3 \ ^2P_J - 2s 2p^4 \ ^2P_{J'}$ multiplet are predicted to lie between 259 and 262 \AA . The strongest is $\lambda 261.208$ which is found in the spectrum; the velocity is consistent with Mg VII which is formed at the same temperature (Table 6) and the DEM predicts the strength of the line to be in excellent agreement with observations. Another line from the same upper level, $\lambda 261.030$, is blended with Si X $\lambda 261.05$ but we estimate that it makes less than a 3 % contribution to this line. The $^2P_{1/2}$ level gives rise to two lines at

259.020 and 259.196 Å, the latter of which is a good wavelength match for the observed line at 259.226 Å. However, Table 3 shows that the observed line is much stronger than expected. There is a known blend with a Cr VII line, but this accounts for only $\simeq 20\%$ of the total observed intensity, with Al VII accounting for $\simeq 15\%$. Al VII $\lambda 259.020$ is predicted to be 83% of the strength of $\lambda 259.196$, but no line can be measured at this wavelength, consistent with $\lambda 259.196$ providing only a small contribution to the measured line at 259.226 Å.

The $2s^2 2p^3 \ ^2P_{1/2,3/2} - 2s 2p^4 \ ^2S_{1/2}$ transitions at 278.960 and 279.164 Å are density sensitive relative to the lines discussed above, but can not be found in the present spectrum. This is consistent with a density of $\leq 10^{10} \text{ cm}^{-3}$.

6.11. Al VIII

Al VIII is isoelectronic with Mg VII and the four strong Mg VII transitions between 276 and 281 Å discussed earlier are found between 247 and 252 Å for Al VIII, although much weaker due to the lower element abundance. The strongest of the $2s^2 2p^2 \ ^3P_J - 2s 2p^3 \ ^3S_1$ multiplet is present in the EIS spectrum at 250.155 Å: the line velocity is in good agreement with the Si VIII lines which have a similar T_{eff} value (Table 6) and the intensity is well reproduced by the DEM. The next strongest line is blended with O V $\lambda 248.46$ and Table 3 shows that Al VIII contributes $\simeq 15\%$ of the total intensity. The third and weakest line of the multiplet is blended with an unknown line at 247.426 Å, which is expected to provide $\simeq 85\%$ of the total intensity.

The density sensitive $2s^2 2p^2 \ ^1D_2 - 2s 2p^3 \ ^1P_1$ transition is expected at 251.36 Å but can not be found in the spectrum. Another density sensitive line is $2s^2 2p^2 \ ^1D_2 - 2s 2p^3 \ ^1D_2$ at 285.46 Å which is around a factor two stronger than $\lambda 251.36$ but it also can not be found in the spectrum. This is consistent with an electron density lower than $\log N_e < 10$.

6.12. Al IX

The only Al IX transitions which provide observable lines in the EIS ranges are those from the $2s^2 2p \ ^2P - 2s 2p^2 \ ^2P$ multiplet, observed in the 280-287 Å wavelength range. The strongest of these lines ($^2P_{3/2} - ^2P_{3/2}$) lies close to the very strong Fe XV line at $\lambda 284.15$ and in active region conditions it is lost under the profile of the latter line. The $^2P - ^2S$ transitions are found just outside the EIS wavelength range at around 300 Å. These lines provide density sensitive intensity ratios in the $7.0 < \log N_e < 8.5$ range.

Three out of four Al IX transitions are identified in the present spectrum, since the

intensity of the weakest line of the multiplet is predicted to be $4.4 \text{ erg cm}^{-2}\text{s}^{-1}\text{sr}^{-1}$ and is not observed. Table 3 shows that the other three lines are only in partial agreement with each other. There is a factor $\simeq 1.7$ difference between the $L(T_{eff})$ values of the $\lambda 284.06$ and the $\lambda 286.38$ lines which can not be accounted for by the uncertainties. The third line falls in between these two so that it is not easy to understand whether the strongest line of the multiplet is blended, or some problem affects the $\lambda 286.38$ line. Density sensitivity is not the cause of the problem, as the $L(T_{eff})$ values of the three lines are closest to each other for $\log N_e > 8.2$, and diverge at lower densities. The Fe xv line is moderately weak at the locations we have selected for the present atlas, so it should be well resolved from the ALIX transition.

6.13. Si vi

The atomic model for Si vi in CHIANTI predicts only two bright emission lines in the EUV, both of which are observed by EIS. A large number of additional lines are predicted to be three or more orders of magnitude less intense and are too weak to be observed by EIS. The strongest line is at 246.01 \AA and we perform a simultaneous three Gaussian fit here in order to pick out two weak lines in the wings of the Si vi line. The longer wavelength line is due to Fe xiii while the short wavelength line is unknown. Note that the widths of each of the three Gaussians were forced to be the same in the fitting process, and thus the Si vi width will dominate, making the line fit parameters for the two weak lines uncertain.

Si vi $\lambda 249.12$ is close to the hot Ni xvii $\lambda 249.18$ line which is very strong in the cores of active regions, but can be neglected in the present spectrum. Another nearby line we believe is due to Fe vii but is clearly separated from the Si vi line. The two Si vi lines form a branching ratio and the predicted intensities are in excellent agreement with the measured values (Table 3).

6.14. Si vii

The only significant lines predicted by CHIANTI in the EIS wavebands belong to the $2s^2 2p^4 \text{ } ^3P_J - 2s 2p^5 \text{ } ^3P_{J'}$ multiplet, which yields six lines between 272 and 279 \AA . Three of these lines are blended but in the case of $\lambda 278.45$ a two Gaussian fit can be used to separate the line from Mg vii $\lambda 278.39$ if both lines are forced to have the same width (Table 4). There are three lines that are emitted by the $2s 2p^5 \text{ } ^3P_1$ level ($\lambda\lambda 272.65, 275.68, 276.85$): $\lambda 276.85$ is blended with two Si viii transitions and Sect. 6.15 demonstrates how Si vii $\lambda 275.68$ was

used to estimate the Si VII contribution to this blend. The two unblended lines, $\lambda 272.65$ and 275.68 , are in good agreement with theory (Table 3). The three lines from the 3P_1 upper level are weakly density sensitive relative to those from the $2s2p^5 {}^3P_2$ level ($\lambda\lambda 275.35, 278.44$). Agreement is found for any density $\log N_e \geq 7.5$.

The remaining Si VII line at 274.18 \AA is emitted from the $2s2p^5 {}^3P_0$ level and shows greater density sensitivity than the other lines. It is blended with Fe XIV $\lambda 274.20$ which is generally much stronger in active regions, but in the present spectrum Si VII dominates, and provides $\simeq 57\%$ of the observed intensity (Table 3) if we assume a density of $\log N_e = 9.15$.

Two more lines are predicted to be bright enough to be observed, and they are both emitted from the $2s2p^5 {}^1P_1$ level. These two lines provide excellent density diagnostic ratios when compared to the 3P – 3P lines discussed above. However, one of them falls in the wavelength gap between the two EIS bands, while the other is expected at 246.12 \AA and is lost under two stronger blending lines of Si VI and Fe XIII.

6.15. Si VIII

Two groups of Si VIII lines are expected in the EIS wavelength ranges: the four $2s^22p^3 {}^2D_J - 2s2p^4 {}^2D_{J'}$ transitions between 276.8 and 277.1 \AA , and the two $2s^22p^3 {}^2P_J - 2s2p^4 {}^2S_{1/2}$ transitions between 250 and 251 \AA . The latter two lines are very weak, but can be measured in the present spectrum and will be discussed towards the end of this section. The four 2D – 2D transitions consist of a pair of strong transitions ($3/2$ – $3/2$, $5/2$ – $5/2$ at 276.85 and 277.06 \AA , respectively), and a pair of weak transitions ($3/2$ – $5/2$, $5/2$ – $3/2$ at 276.87 and 277.04 \AA , respectively). These lines are blended with lines of Mg VII and Si VII making it difficult to extract the Si VIII line intensities, and we describe in detail below the method used here.

Fig. 9 shows the EIS spectrum in the vicinity of the Si VIII 2D – 2D transitions, with the different ion species and lines indicated. Attempts to fit the lines simultaneously with multiple Gaussians each with three free parameters (line peak, centroid and width) fail due to the number of lines (7) between 276.8 and 277.3 \AA . The fitting process can be simplified significantly by making use of the nearby Si VII $\lambda 275.68$ and Mg VII $\lambda 276.14$ lines, which have fixed separations and ratios relative to the Si VII and Mg VII lines blending with the Si VIII lines.

The Si VII $\lambda 276.85/\lambda 275.68$ branching ratio is 1.3. Also the separation of the two lines is accurately known from measurements of the $2s^22p^4 {}^3P_1 - {}^3P_0$ transition at infrared wavelengths (Feuchtgruber et al. 1997). We thus allow the isolated $\lambda 275.68$ line to be freely fit,

and then force $\lambda 276.85$ to have the same width (since the lines arise from the same ion), a peak 1.31 times that of $\lambda 275.68$, and a separation of 1.176 \AA . Similarly, Mg VII $\lambda 276.99/\lambda 276.14$ has a branching ratio of 2.99, and the wavelength separation is accurately known from infrared measurements of the $2s^2 2p^2 \ ^3P_0 - \ ^3P_1$ wavelength (Kelly & Lacy 1995). The isolated $\lambda 276.14$ line is then used to determine the $\lambda 276.99$ parameters.

For Si VIII, each of the four emission lines is forced to have the same width, but this width is free to vary. The peaks and centroids of the two strong lines, $\lambda 276.85$ and $\lambda 277.06$, are free to vary, but those of the two weak lines, $\lambda 276.87$ and $\lambda 277.04$, are fixed relative to these lines. $\lambda 276.85$ and $\lambda 277.04$ share a common upper level and they have a branching ratio of 0.087 (using the atomic data of Zhang & Sampson 1999), while their wavelength separation is accurately determined to be 0.193 \AA from the separation of the Si VIII, $\lambda \lambda 1440, 1445$ transitions in the far ultraviolet. Similarly $\lambda 277.06$ and $\lambda 276.87$ share a common upper level and have a branching ratio of 0.040, while their wavelength separation is also 0.193 \AA .

Two additional Gaussians are added to fit Mg V $\lambda 276.58$ and Si X $\lambda 277.26$, each having completely free parameters. In summary, the spectral region between 275.55 and 277.50 \AA is fit with 10 Gaussians together with a straight line for the background. There are 21 free parameters in all, and the reduced χ^2 value for the fit is 2.3. The complete fit function is displayed in Fig. 9 and Table 4 gives the line fit parameters for each of the 10 emission lines.

The wavelength separation of the two strong Si VIII lines is $0.201 \pm 0.003 \text{ \AA}$ which is close to the value from Edlén (1984) of 0.207 \AA , while Table 6 shows that the velocities of the two lines are in good agreement with Al VIII. Note that there appears to be a jump in the spectrum redshift between the ions formed at $\log T < 5.8$ and those formed at $\log T > 5.8$ of about 20 km s^{-1} .

The two $2s^2 2p^3 \ ^2P_J - 2s 2p^4 \ ^2S_{1/2}$ transitions have rest wavelengths of 250.47 and 250.81 \AA and two weak lines are found close to these wavelengths in the spectrum. The velocity of $\lambda 250.81$ is consistent with $\lambda 276.86$ and $\lambda 277.06$ (Table 6), giving confidence in the identification. $\lambda 250.47$ is predicted to be a factor 0.65 of the strength of $\lambda 250.81$, in good agreement with observations. However, the line is very narrow and the velocity is significantly discrepant with the other Si VIII lines (Table 6). There is considerable density sensitivity in the Si VIII lines, and the L-function method shows best agreement among all lines for $\log N_e = 9.05 \pm 0.30$.

Si VIII emits several other strong spectral lines in the $214\text{--}236 \text{ \AA}$ wavelength range that are useful for plasma diagnostics. Unfortunately, they all fall in the wavelength gap between the two EIS bands and can not be used.

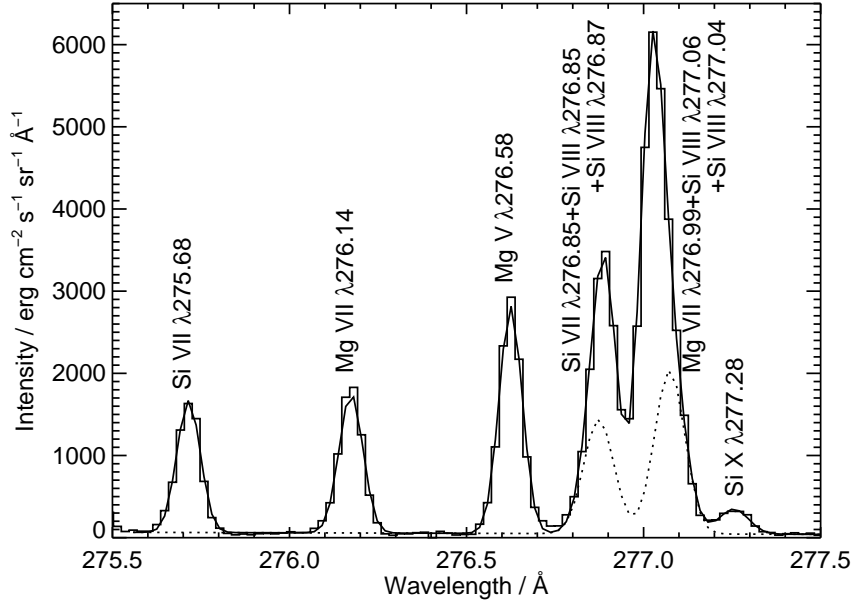


Fig. 9.— The EIS spectrum from 275.5 to 277.5 Å showing the emission lines that were simultaneously fit in order to derive line fit parameters for Si VIII. The spectrum is shown as a histogram plot and the complete fit function is overlaid as a smooth, complete line. The Si VIII components of the fit function are overlaid as a dotted line.

6.16. Si IX

The only lines expected to be found in the EIS wavebands based on the CHIANTI atomic model are at 258.08 and 290.69 Å, and both are measured here. $\lambda 258.08$ is unblended but $\lambda 290.69$ lies in the wing of a stronger Fe VII line, and the combined feature was fit with two Gaussians forced to have the same width. These lines are strongly density sensitive relative to each other and the CHIANTI Si IX model yields a value of $\log N_e = 9.20 \pm 0.30$.

Other strong lines are predicted to fall in the $\lambda\lambda 220$ – 230 wavelength range, that can not be observed with EIS.

6.17. S VIII

The $2s^2 2p^5 \ ^2P_{3/2,1/2} - 2s 2p^6 \ ^2S_{1/2}$ doublet lines, $\lambda\lambda 198.55, 202.61$, are found in the EIS short wavelength band and both are blended with Fe XI transitions. Thus, the results in Table 3 can not be put in an absolute scale. However, the derived DEM demonstrates that

S VIII provides the dominant contribution in both cases (Table 4). Brown et al. (2008) also listed a Fe XII line as blending with S VIII $\lambda 198.55$, but we find the predicted intensity for this line is negligible when using the DEM. If we use the reference wavelengths of Robinson (1937) for S VIII, then the derived velocities are $+24.1 \text{ km s}^{-1}$ and $+22.2 \text{ km s}^{-1}$ for $\lambda 198.55$ and $\lambda 202.61$, respectively, which are consistent with the Si VIII and Al VIII velocities (Table 6) and also confirm that S VIII provides a dominant contribution to both lines. Note that S VIII has an effective temperature of $\log T_{\text{eff}} = 5.83$, placing it between Si VII and Si VIII.

Since the S VIII lines may be valuable for abundance studies (e.g., Feldman et al. 2009) we note that the Fe XI contributions can more generally be estimated through branching ratios. Using the atomic data from CHIANTI, $\lambda 198.55/\lambda 189.14$ has a theoretical ratio of 0.80, while $\lambda 202.63/\lambda 188.23$ has a ratio of 0.016. $\lambda 188.23$ is the strongest Fe XI line observed by EIS, and $\lambda 189.14$ appears to be unblended.

6.18. Cr VII

Cr VII lines have been identified in laboratory spectra (Gabriel et al. 1966; Ekberg 1976), but never previously seen in solar spectra. The ion is isoelectronic with Fe IX and the analogous transition to the strong $\lambda 171.07$ line of Fe IX is found at 202.83 \AA , which matches a strong line at this wavelength. An image formed from the line looks similar to Fe VII and Fe VIII images, which is consistent with the predicted temperature of maximum ionization, $\log T_{\text{max}} = 5.7$, of Cr VII. In addition, using the laboratory wavelength of Ekberg (1976) yields a velocity of $+42.9 \text{ km s}^{-1}$, in good agreement with Si VII which is formed at a similar temperature (Table 6). Brown et al. (2008) identify the O IV $\lambda 202.885$ line in their spectra which is close in wavelength to the Cr VII line, however the CHIANTI model for O IV predicts this transition to be around a factor 40 weaker than O IV $\lambda 279.933$ and so in the present spectrum it can safely be ignored. Landi & Young (2009) have computed new atomic data for Cr VII and the emission measure distribution yields a line intensity in reasonable agreement with the observations considering the uncertainties in the atomic calculations. We are thus confident that the 202.83 \AA emission line is due to Cr VII.

By comparing with the Fe IX atomic model, we expect also to find additional lines at 258.65 , 259.18 , 261.31 and 288.90 \AA that will be around 5–20 % of the $\lambda 202.83$ line. There are indeed lines at these wavelengths except at $\lambda 288.90$; Table 3 shows that all these weaker lines are brighter than predicted. Two of these lines are predicted to be strongly density sensitive but no common crossing point can be identified: Table 3 results have been obtained assuming that $\log N_e = 9.15$. No clear candidates for blending are available for any of the lines except $\lambda 259.18$, which is blended by an Al VII line (Section 6.10). Also, they are too

weak to provide an intensity map that can be matched with a temperature class, so the identification of these lines remains to be confirmed.

6.19. Cr VIII

With the identification of Cr VII $\lambda 202.83$, we also expect to find Cr VIII $\lambda 205.01$ which is the analogous transition to the strong $\lambda 174.53$ line of Fe X. A line is found at 205.05 \AA which is around a factor 2 weaker than $\lambda 202.83$ and, based on image inspection, is formed close to Fe VII and Fe VIII. We thus identify this with Cr VIII. Converting the measured wavelength to a velocity gives $+62.9 \text{ km s}^{-1}$, significantly different to Si VIII and Al VIII which are formed at a similar temperature (Table 6). However, the reference wavelengths for Cr VIII come from the laboratory spectra obtained by Fawcett & Gabriel (1966) but are only accurate to $\pm 0.05 \text{ \AA}$ (see also Gabriel et al. 1966).

Other Cr VIII lines are found in the EIS range, and the comparison with $\lambda 205.01$ is reported in Table 3. Good agreement is found; the lines are also density sensitive relative to each other, and the best agreement is found for $\log N_e = 9.45$, a bit higher than the values found for other ions. The $\lambda 211.48$ is also reported as Ni XI: while Ni XI is predicted to provide $\simeq 50\%$ of the total intensity, Cr VIII accounts for all of it. The reason for this discrepancy is not clear, but it is likely to be found in the atomic data.

6.20. Mn VIII

Mn VIII is isoelectronic with Fe IX, and its spectrum is also dominated by the strong singlet transition $3s^2 3p^6 \text{ } ^1\text{S} - 3s^2 3p^5 3d \text{ } ^1\text{P}$, which is identified as $\lambda 185.462$. Using the new atomic data from Landi & Young (2009), the predicted intensity of this line agrees well with observations, however the velocity derived using the reference wavelength of Smitt & Svensson (1983) is discrepant with other ions of the same temperature such as Si VII and Mg VII by around 20 km s^{-1} . The velocity instead is more consistent with the hotter ions Si VIII and Al VIII, perhaps suggesting the ion balance for Mn VIII is yielding too low a temperature.

Other, weaker Mn VIII lines are predicted to fall in the EIS wavelength ranges, the strongest of which is identified at 263.200 \AA with a weak line whose intensity map is consistent with a cool line. Table 3 reports the comparison between the two lines. They are strongly density sensitive for $\log Ne > 9.5$, but at lower densities their ratio is more constant; $\lambda 263.20$ is brighter than predicted by the comparison with the strong singlet line, so that some unidentified blend has to provide almost 60% of the total observed intensity.

6.21. Mn IX

Using the atomic data of Landi & Young (2009), the DEM yields three Mn IX lines that are potentially observable in the present spectrum, and wavelength matches are found for each. $\lambda 188.48$ is the strongest line and is the analogous transition to Fe X $\lambda 174.53$. It lies in a crowded part of the spectrum and it could provide a contribution to either Fe VII $\lambda 188.40$ or Fe IX $\lambda 188.50$ (observed at 188.425 and 188.507 Å, respectively). The reference wavelength (due to Fawcett & Gabriel 1966) is only accurate to ± 0.05 Å and so it is not possible to clearly identify Mn IX with either of the observed lines. We note, however, that Young & Landi (2009) find that Fe VII does not fully account for the strength of the observed line at 188.425 Å and so in Table 4 we identify Mn IX with this line.

The two other potential Mn IX identifications are $\lambda 191.60$ and $\lambda 199.32$ which are the analogous transitions to Fe X $\lambda 177.24$ and $\lambda 184.54$, respectively. Using the Fawcett & Gabriel (1966) reference wavelengths yields velocities of $+18.8$ and $+7.5$ km s $^{-1}$, respectively, which give confidence in the identifications although we note again the low precision of the laboratory wavelengths. The intensities predicted from the DEM are significantly below the observed intensities, however images formed in both the lines are consistent with the expected formation temperature of Mn IX ($\log T_{\text{eff}} = 5.86$). Given the uncertainties in the identifications and blends, the results in Table 3 can not be put on an absolute scale.

New, more precise, laboratory wavelength measurements would be valuable for confirming the Mn IX identifications.

6.22. Ni XI

Ni XI has the same atomic structure as Fe IX and its spectrum is dominated by the strong singlet line, analogous to Fe IX $\lambda 171.07$, which lies outside the EIS wavelength range. Three Ni XI lines are identified in this spectrum, one of which for the first time as blending an Al V transition at $\lambda 278.73$. Ni XI is expected to provide $\simeq 13\%$ of the total intensity, bringing the combined predicted intensity of the blended feature much closer to observations. Due to the Al V blend, the identification of this line does not allow us to determine an accurate wavelength for this transition and calculate from it the energy of the upper level.

The other two lines are identified near the edge of the EIS short wavelength band. These two lines are analogous to Fe IX $\lambda\lambda 241.74, 244.91$, which have been observed in the past and used for density diagnostics due to the strong density sensitivity of their intensity ratio. In the present spectrum, $\lambda 211.48$ is blended with a Cr VIII transition. Some problem is found here, as the Cr VIII line accounts for all the observed intensity, while Table 3 predicts Ni XI

to provide $\simeq 50\%$ of the total intensity.

7. Conclusions

In the present work we have analyzed a full EIS spectral scan of a portion of an active region where the plasma emission was enhanced at transition region temperatures. We first measured the DEM and electron density of the plasma, and used the results to develop a complete atlas of the emitting spectrum, and to compare observed line intensities with predicted values from the CHIANTI database. The Fe VII-IX lines measured in the present spectrum have been analyzed in a separate paper (Young & Landi 2009).

While most of the lines identified in the spectrum were observed in other occasions by EIS, the strong enhancement of the emission at temperatures in the $\log T = 5.5\text{--}5.9$ range has allowed us to identify several lines never observed in solar spectra. These lines, sometimes identified in laboratory spectra, are usually too faint to be detected but in special plasmas like the one we studied can provide valuable diagnostic tools to measure the physical properties of the emitting plasma.

The observed spectrum was also used to carry out a systematic assessment of the accuracy of CHIANTI emissivities, as well as of the diagnostic application, for transition region ions. The brightness of the transition region emission has allowed us to carry out such a comparison including more lines and ions and with better accuracy than possible with standard active region or quiet Sun spectra.

We find that CHIANTI emissivities are almost always in excellent agreement with observations. We identified blends for several lines, and discussed the diagnostic application of many of the lines reported in the present atlas.

The work of EL is supported by the NNG06EA14I, NNH06CD24C and other NASA grants.

REFERENCES

- Artru, M.-C., & Brillet, W.-Ü. L. 1974, *J. Opt. Soc. America*, 64, 1063
- Artru, M.-C., & Brillet, W.-Ü. L. 1977, *Phys. Scripta*, 16, 93
- Brown, C. M., Hara, H., Kamio, S., *et al.* 2007, *PASJ*, 59, S865

- Brown, C. M., Feldman, U., Seely, J. F., Korendyke, C. M., & Hara, H. 2008, *ApJS*, 176, 511
- Bryans, P., Landi, E., & Savin, D. W. 2009, *ApJ*, 691, 1540
- Culhane, J. L., Harra, L. K., James, A. M., et al. 2007, *Solar Physics*, 243, 19
- Dere, K. P., Landi, E., Mason, H. E., Monsignori-Fossi, B. C., & Young, P. R. 1997, *A&AS*, 125, 149
- Dere, K. P., Landi, E., Young, P. R., Del Zanna, G., Landini, M., & Mason, H. E. 2009, *A&A*, 498, 915
- Edlén, B. 1934, *Nova Acta Reg. Soc. Sci. Uppsala (Iv)* 9, No. 6
- Edlén, B. 1979, *Phys. Scripta*, 19, 255
- Edlén, B. 1983, *Phys. Scripta*, 28, 51
- Edlén, B. 1984, *Phys. Scripta*, 30, 135
- Edlén, B. 1985, *Phys. Scripta*, 31, 345
- Ekberg, J. O. 1976, *Phys. Scripta*, 13, 245
- Ekberg, J. O. 1981, *Phys. Scripta*, 23, 7
- Fawcett, B. C., & Gabriel, A. H. 1966, *Proc. Phys. Soc. (London)*, 88, 262
- Feldman, U., Mandelbaum, P., Seely, J. L., Doschek, G. A., & Gursky H. 1992, *ApJSS*, 81, 387
- Feldman, U., Warren, H. P., Brown, C. M., & Doschek, G. A. 2009, *ApJ*, 695, 36
- Feuchtgruber, H., Lutz, D., Beintema, D. A., et al. 1997, *ApJ*, 487, 962
- Gabriel, A. H., Fawcett, B. C., & Jordan, C. 1966, *Proc. Phys. Soc.*, 87, 825
- Günther, H. M., & Schmitt, J. H. M. M. 2008, *A&A*, 481, 735
- Kelly, D. M., & Lacy, J. H. 1995, *ApJ*, 454, L161
- Ko, Y.-K., Doschek, G. A., Warren, H. P., & Young, P. R. 2009, *ApJ*, 697, 1956
- Kosugi, T., Matsuzaki, K., Sakao, T., et al. 2007, *Sol. Phys.*, 243, 3

- Landi, E., & Landini, M. 1997, *A&A*, 327, 1230
- Landi, E., Feldman, U., & Dere, K. P. 2002a, *ApJS*, 139, 281
- Landi, E., Feldman, U., & Dere, K. P. 2002b, *ApJ*, 574, 495
- Landi, E., & Phillips, K. J. H. 2006, *ApJS*, 166, 421
- Landi, E., & Young, P. R. 2009, *ApJ*, in preparation
- Ramonas, A. A., & Ryabtsev, A. N. 1980, *Opt. Spect.*, 48, 348
- Reyes-Iturbide, J., Rosado, M. & Velázquez, P. F. 2008, *AJ*, 136, 2011
- Robinson, H. A. 1937, *Phys. Rev.*, 52, 724
- Sallmen, S. M., Korpela, E. J., & Yamashita, H. 2008, *ApJ*, 681, 1310
- Smitt, R. & Svensson, L. Å 1983 *Phys. Scripta*, 27, 364
- Steffl, A. J., Delamere, P. A., & Bagenal, F. 2008, *Icarus*, 194, 153
- Young, P. R., Landi, E., & Thomas, R. J. 1998, *A&A*, 329, 291
- Young, P. R., Del Zanna, G., Mason, H. E., et al. 2007a, *PASJ*, 59, S727
- Young, P. R., Del Zanna, G., Mason, H. E., et al. 2007b, *PASJ*, 59, S857
- Young, P. R., Watanabe, T., Hara, H., & Mariska, J. T. 2009, *A&A*, 495, 587
- Young, P. R. 2009, *ApJ*, 691, L77
- Young, P. R., & Landi, E. 2009, *ApJ*, submitted
- Zhang, H. L., & Sampson, D. H. 1999, *ADNDT*, 72, 153

Table 4. Line list. λ and σ_λ are the line wavelength and its uncertainty (in Å and mÅ, respectively); I and σ_I are the line intensity and its uncertainty (in $\text{erg cm}^{-2}\text{s}^{-1}\text{sr}^{-1}$; W and σ_W are the line width and its uncertainty (in mÅ). For some strong lines, $\sigma_\lambda < 0.5$ mÅ and so the rounded σ_λ given in the table is 0.

λ	σ_λ	I	σ_I	W	σ_W	Class	Ion	λ_{ref}	Ref.	Transition	$\log T_{\text{max}}$	I_{pred}
171.070	1	6779.7	356.2	83.7	1.1	E	Fe IX	171.073	1	$3s^2 3p^6 \ ^1S_0 - 3s^2 3p^5 3d \ ^1P_1$	5.7	9070.0
172.926	15	199.5	108.4	63.1	34.3		O VI	172.936	1	$2p \ ^2P_{1/2}^o - 3d \ ^2D_{3/2}$	5.6	105.0
173.120	17	300.5	127.4	99.3	42.1		O VI	173.080	1	$2p \ ^2P_{3/2}^o - 3d \ ^2D_{5/2}$	5.6	190.0
							O VI	173.095	1	$2p \ ^2P_{3/2}^o - 3d \ ^2D_{3/2}$	5.6	21.0
174.523	1	1810.5	87.9	88.6	1.1	F	Fe X	174.531	1	$3s^2 3p^5 \ ^2P_{3/2}^o - 3s^2 3p^4 ({}^3P) 3d \ ^2D_{5/2}$	6.0	1750.0
175.265	1	232.8	12.4	76.7	1.1		Fe X	175.263	1	$3s^2 3p^5 \ ^2P_{1/2}^o - 3s^2 3p^4 ({}^3P) 3d \ ^2D_{3/2}$	6.0	260.0
176.762	4	191.4	32.7	57.9	9.5		Fe VII	176.744	3	$3p^6 3d^2 \ ^3F_4 - 3p^5 3d^3 ({}^4F) \ ^3F_4^o$	5.6	108.0
176.968	4	446.7	42.8	109.5	10.1		Fe IX	176.959	2	$3s^2 3p^5 3d \ ^3F_4^o - 3s^2 3p^4 ({}^1D) 3d^2 \ ^3D_3$	5.7	274.0
							Fe VII	176.928	3	$3p^6 3d^2 \ ^3F_3 - 3p^5 3d^3 ({}^4F) \ ^3F_3^o$	5.6	74.5
177.236	2	1101.9	52.8	80.3	3.3	F	Fe X	177.240	1	$3s^2 3p^5 \ ^2P_{3/2}^o - 3s^2 3p^4 ({}^3P) 3d \ ^2P_{3/2}$	6.0	957.0
							Fe VII	177.172	3	$3p^6 3d^2 \ ^3F_2 - 3p^5 3d^3 ({}^4F) \ ^3F_2^o$	5.6	52.9
							Fe IX	177.594	2	$3s^2 3p^5 3d \ ^3F_3^o - 3s^2 3p^4 ({}^1D) 3d^2 \ ^3D_2$	5.7	139.0
177.603	6	148.2	26.1	86.9	15.3							
178.708	2	68.5	5.0	84.5	4.1							
178.994	3	76.0	5.2	115.5	5.5							
179.245	2	45.8	4.0	60.3	3.6							
179.740	3	56.3	4.7	108.5	6.2	G	Fe XI	179.764	1	$3s^2 3p^4 \ ^1D_2 - 3s^2 3p^3 ({}^2D) 3d \ ^1F_3$	6.0	35.2
180.402	1	840.8	43.8	95.9	1.9	G	Fe XI	180.408	1	$3s^2 3p^4 \ ^3P_2 - 3s^2 3p^3 ({}^4S) 3d \ ^3D_3$	6.0	739.0
							Fe X	180.441	1	$3s^2 3p^5 \ ^2P_{1/2}^o - 3s^2 3p^4 ({}^3P) 3d \ ^2P_{1/2}$	6.0	148.0
180.618	4	34.6	3.8	74.7	6.9	G	Fe XI	180.600	1	$3s^2 3p^4 \ ^3P_1 - 3s^2 3p^3 ({}^4S) 3d \ ^3D_1$	6.0	42.5
181.119	3	34.1	3.9	74.7	6.8	G	Fe XI	181.137	1	$3s^2 3p^4 \ ^3P_0 - 3s^2 3p^3 ({}^4S) 3d \ ^3D_1$	6.0	59.7
181.374	5	16.8	2.8	66.2	9.9							
181.622	12	12.4	5.2	67.4	28.1							
181.744	6	22.2	5.1	65.3	15.0							
182.099	9	23.1	8.8	56.0	0.0		Fe VII	182.071	3	$3p^6 3d^2 \ ^3F_4 - 3p^5 3d^3 ({}^2F) \ ^3D_3^o$	5.6	4.7
182.171	3	151.3	13.7	79.2	7.2	G	Fe XI	182.169	1	$3s^2 3p^4 \ ^3P_1 - 3s^2 3p^3 ({}^4S) 3d \ ^3D_2^o$	6.0	149.0
182.308	3	58.2	7.2	75.3	9.2	F	Fe X	182.307	1	$3s^2 3p^5 \ ^2P_{1/2}^o - 3s^2 3p^4 ({}^3P) 3d \ ^2P_{3/2}$	6.0	25.8
182.430	7	21.6	5.5	68.3	17.2							
182.755	7	10.7	3.6	54.5	18.5							
182.946	7	26.2	4.7	93.0	16.9							
183.163	8	11.6	4.3	60.6	22.3							
183.345	6	13.0	3.1	57.3	13.5							
183.467	7	11.5	3.2	62.5	17.5							
183.566	5	12.0	2.8	47.9	11.2		Fe VII	183.539	3	$3p^6 3d^2 \ ^3P_1 - 3p^5 3d^3 ({}^4P) \ ^3P_2^o$	5.6	8.9
183.849	2	90.9	5.4	65.5	3.9	C	Fe VII	183.825	3	$3p^6 3d^2 \ ^3P_2 - 3p^5 3d^3 ({}^4P) \ ^3P_2^o$	5.6	33.0
183.951	2	96.1	5.4	68.8	3.9	A	O VI	183.939	9	$1s^2 2p \ ^2P_{1/2}^o - 1s^2 3s \ ^2S_{1/2}$	5.6	65.8
184.141	1	145.3	5.9	74.2	2.5	A	O VI	184.119	9	$1s^2 2p \ ^2P_{3/2}^o - 1s^2 3s \ ^2S_{1/2}$	5.6	132.0
184.426	4	36.4	4.6	70.0	8.9	F	Fe XI	184.412	1	$3s^2 3p^4 \ ^1S_0 - 3s^2 3p^3 ({}^2P) 3d \ ^1P_1^o$		1.4
184.542	1	504.3	9.2	76.7	1.2	F	Fe X	184.537	1	$3s^2 3p^5 \ ^2P_{3/2}^o - 3s^2 3p^4 ({}^1D) 3d \ ^2S_{1/2}$	6.0	397.0
184.777	3	36.3	3.1	70.0	6.0		Ne V	184.735	1	$2s^2 2p^2 \ ^1S_0 - 2s^2 2p 3s \ ^1P_1$	5.6	7.7
							Fe XI	184.803	1	$3s^2 3p^4 \ ^1D_2 - 3s^2 3p^3 ({}^2D) 3d \ ^1D_2$	6.0	21.3
							Fe VII	184.752	3	$3p^6 3d^2 \ ^3F_0 - 3p^5 3d^3 ({}^4P) \ ^3P_1^o$	5.6	8.3
184.922	3	20.2	2.8	61.9	8.6		Ne VI	184.945	1	$2s^2 2p^2 \ ^2S_{1/2} - 2s^2 3p \ ^2P_{3/2}^o$	5.7	8.7
							Fe VII	184.886	3	$3p^6 3d^2 \ ^3P_1 - 3p^5 3d^3 ({}^4P) \ ^3P_1^o$	5.6	7.8
185.232	0	1503.2	13.8	67.8	0.4	D	Fe VIII	185.213	14	$3p^6 3d \ ^2D_{5/2} - 3p^5 3d^2 ({}^3F) \ ^2F_{7/2}^o$	5.7	2760.0
185.467	2	116.9	5.3	87.0	3.9	C-D	Mn VIII	185.455	12	$3s^2 3p^6 \ ^1S_0 - 3s^2 3p^5 3d \ ^1P_1^o$	5.7	105.0
185.574	2	66.1	3.9	59.6	3.6	B-C	Fe VII	185.547	3	$3p^6 3d^2 \ ^1D_2 - 3p^5 3d^3 ({}^2G) \ ^1F_3^o$	5.6	36.0
185.780	10	7.7	2.1	79.9	9.0		O V	185.745	1	$2s 2p \ ^1P_1^o - 2p 3p \ ^1D_2^o$	5.6	3.3
186.004	5	18.5	2.6	79.9	9.0	C-E						
186.142	7	12.4	2.2	79.9	9.0							
186.624	1	1139.9	14.0	67.4	0.8	D	Fe VIII	186.601	14	$3p^6 3d \ ^2D_{3/2} - 3p^5 3d^2 ({}^3F) \ ^2F_{5/2}^o$	5.7	1890.0
186.692	6	43.8	7.2	53.7	8.2		Fe VII	186.657	3	$3p^6 3d^2 \ ^1D_2 - 3p^5 3d^3 ({}^2D) \ ^1D_2^o$	5.6	34.4
186.877	1	174.2	4.3	93.1	2.3	H	Fe XII	186.854	1	$3s^2 3p^3 \ ^2D_{3/2}^o - 3s^2 3p^2 ({}^3P) 3d \ ^2F_{5/2}$	6.1	26.5
							Fe XII	186.887	1	$3s^2 3p^3 \ ^2D_{5/2}^o - 3s^2 3p^2 ({}^3P) 3d \ ^2F_{7/2}$	6.1	95.8
							Fe VII	186.868	3	$3p^6 3d^2 \ ^3P_2 - 3p^5 3d^3 ({}^2G) \ ^1F_3^o$	5.6	7.9
187.181	35	16.1	10.6	103.7	68.6							
187.264	3	114.0	10.5	66.9	4.4	C	Fe VIII	187.237	14	$3p^6 3d \ ^2D_{5/2} - 3p^5 3d^2 ({}^3F) \ ^2F_{5/2}^o$	5.7	86.4
							Fe VII	187.235	3	$3p^6 3d^2 \ ^1D_2 - 3p^5 3d^3 ({}^2F) \ ^3D_3^o$	5.6	9.0
187.433	7	11.6	3.1	81.5	21.5							
187.562	8	9.0	2.5	75.2	21.0							
187.714	2	22.3	2.6	63.8	7.5	B	Fe VII	187.692	3	$3p^6 3d^2 \ ^3P_1 - 3p^5 3d^3 ({}^2D) \ ^1D_2^o$	5.6	4.4
187.848	5	7.1	1.8	58.2	15.2							
187.971	1	89.8	3.3	89.8	3.1	E						
188.144	10	42.5	10.5	95.0	0.0							
188.216	1	386.6	18.2	78.6	3.7	G	Fe XI	188.232	1	$3s^2 3p^4 \ ^3P_2 - 3s^2 3p^3 ({}^2D) 3d \ ^3P_2^o$	6.0	361.0
188.303	2	257.0	12.2	77.0	3.6	G	Fe XI	188.299	1	$3s^2 3p^4 \ ^3P_2 - 3s^2 3p^3 ({}^2D) 3d \ ^1P_1$	6.0	131.0
188.424	3	71.8	7.6	66.7	7.1	C	Mn IX	188.480	1	$3s^2 3p^5 \ ^2P_{3/2}^o - 3s^2 3p^4 ({}^3P) 3d \ ^2D_{5/2}$	6.0	21.6
							Fe VII	188.396	3	$3p^6 3d^2 \ ^1D_2 - 3p^5 3d^3 ({}^2F) \ ^3D_2^o$	5.6	12.5

Table 4—Continued

λ	σ_λ	I	σ_I	W	σ_W	Class	Ion	λ_{ref}	Ref.	Transition	$\log T_{\text{max}}$	I_{pred}
188.507	1	375.5	13.2	70.2	2.5	E	Fe IX	188.497	16	$3s^2 3p^5 3d^3 F_4 - 3s^2 3p^4 ({}^3P) 3d^2 {}^3G_5$	5.7	396.0
188.603	3	72.6	10.7	69.1	10.2	C	Fe VII	188.576	3	$3p^6 3d^2 {}^3P_2 - 3p^5 3d^3 ({}^2F) {}^3D_3^o$	5.6	36.6
188.685	7	31.7	8.0	72.8	18.3	E,H	Fe IX	188.686	1	$3s^2 3p^5 3d^3 F_4 - 3s^2 3p^4 ({}^3P) 3d^2 {}^3G_4$	5.7	22.2
188.768	15	7.5	2.7	56.0	0.0							
188.833	4	42.9	3.8	75.2	6.7							
189.001	3	22.0	2.4	86.1	9.3							
189.127	21	17.7	7.0	74.4	29.4	G	Fe XI	189.130	1	$3s^2 3p^4 {}^3P_1 - 3s^2 3p^3 ({}^2D) 3d {}^3P_1^o$	6.0	25.0
189.359	1	30.5	1.7	60.6	3.4							
189.481	1	53.1	2.1	66.7	2.7	B	Fe VII	189.450	3	$3p^6 3d^2 {}^3P_1 - 3p^5 3d^3 ({}^2F) {}^3D_2^o$	5.6	19.5
189.596	4	8.0	1.6	51.6	10.1	E	Fe IX	189.582	1	$3s^2 3p^5 3d^3 F_3^o - 3s^2 3p^4 ({}^3P) 3d^2 {}^3G_3$	5.7	26.0
189.715	5	6.3	1.5	52.7	13.0	G	Fe XI	189.719	1	$3s^2 3p^4 {}^3P_0 - 3s^2 3p^3 ({}^2D) 3d {}^3P_1^o$	6.0	19.2
189.952	1	236.7	4.8	74.8	1.5	E	Fe IX	189.941	16	$3s^2 3p^5 3d^3 F_3 - 3s^2 3p^4 ({}^3P) 3d^2 {}^3G_4$	5.7	241.0
190.046	1	181.9	4.4	72.0	1.8	F	Fe X	190.037	1	$3s^2 3p^5 {}^2P_{1/2}^o - 3s^2 3p^4 ({}^1D) 3d {}^2S_{1/2}$	6.0	112.0
190.164	5	3.4	1.0	43.9	13.3							
190.359	4	18.2	2.1	74.4	1.9							
190.909	5	19.2	2.4	76.6	1.6							
191.041	11	7.1	1.9	76.6	1.6	H	Fe XII	191.049	1	$3s^2 3p^3 {}^2P_{3/2}^o - 3s^2 3p^2 ({}^3P) 3d {}^2D_{5/2}$	6.1	5.3
191.227	2	105.2	6.7	76.6	1.6	E,H	Fe IX	191.216	16	$3s^2 3p^5 3d^3 F_2 - 3s^2 3p^4 ({}^3P) 3d^2 {}^3G_3$	5.7	105.0
191.411	7	11.5	2.1	76.6	1.6							
191.612	4	37.7	3.5	76.6	1.6	D	Mn IX	191.630	1	$3s^2 3p^5 {}^2P_{3/2}^o - 3s^2 3p^4 ({}^3P) 3d {}^2P_{3/2}$	6.0	10.4
191.707	13	8.5	2.2	76.6	1.6							
191.814	10	8.9	2.0	76.6	1.6							
192.026	3	86.5	6.8	76.6	1.6	D,H	Fe VIII	192.004	14	$3p^6 3d {}^2D_{3/2} - 3p^5 3d^2 ({}^1S) {}^2P_{1/2}^o$	5.7	42.5
							Fe VII	192.006	3	$3p^6 3d^2 {}^1D_2 - 3p^5 3d^3 (a {}^2D) {}^1D_2^o$	5.6	3.0
192.114	4	60.4	5.8	76.6	1.6							
192.313	7	32.2	5.9	76.6	1.6							
192.386	3	100.5	8.2	76.6	1.6	H	Fe XII	192.394	1	$3s^2 3p^3 {}^4S_{3/2}^o - 3s^2 3p^2 ({}^3P) 3d {}^4P_{1/2}$	6.1	135.0
192.642	1	76.7	2.0	74.2	1.9	E-F						
192.777	1	14.4	0.3	65.5	1.4		O V	192.750	1	$2s 2p {}^3P_0^o - 2s 3d {}^3D_1$	5.6	17.0
192.808	1	101.3	2.7	79.8	2.1	G	Fe XI	192.830	1	$3s^2 3p^4 {}^3P_1 - 3s^2 3p^3 ({}^2D) 3d {}^3P_2$	6.1	75.3
192.824	1	27.0	0.6	65.5	1.4		O V	192.797	1	$2s 2p {}^3P_1^o - 2s 3d {}^3D_2$	5.6	30.7
192.828	1	10.8	0.2	65.5	1.4		O V	192.801	1	$2s 2p {}^3P_1^o - 2s 3d {}^3D_1$	5.6	12.7
192.931	1	82.2	1.9	65.5	1.4	A	O V	192.904	1	$2s 2p {}^3P_2^o - 2s 3d {}^3D_3$	5.6	99.7
192.938	1	9.0	0.2	65.5	1.4		O V	192.911	1	$2s 2p {}^3P_2^o - 2s 3d {}^3D_2$	5.6	10.2
193.721	2	71.2	5.6	94.4	5.0	F	Fe X	193.715	1	$3s^2 3p^5 {}^2P_{3/2}^o - 3s^2 3p^4 ({}^1S) 3d {}^2D_{5/2}$	6.0	23.4
193.988	2	44.7	4.3	60.7	3.9	D	Fe VIII	193.967	14	$3p^6 3d {}^2D_{3/2} - 3p^6 4p {}^2P_{3/2}^o$	5.7	53.2
194.319	5	12.8	2.2	72.5	12.2							
194.680	0	457.9	4.1	65.9	0.4	D	Fe VIII	194.662	14	$3p^6 3d {}^2D_{5/2} - 3p^6 4p {}^2P_{3/2}^o$	5.7	524.0
194.816	1	109.0	2.2	91.0	1.9	C-E						
195.115	1	403.6	23.2	96.1	2.6	H	Fe XII	195.119	1	$3s^2 3p^3 {}^4S_{3/2}^o - 3s^2 3p^2 ({}^3P) 3d {}^4P_{5/2}$	6.1	421.0
							Fe XII	195.179	1	$3s^2 3p^3 {}^2D_{3/2}^o - 3s^2 3p^2 ({}^1D) 3d {}^2D_{3/2}$	6.1	12.0
195.415	0	224.8	3.0	64.0	0.8	C	Fe VII	195.391	3	$3p^6 3d^2 {}^3F_4 - 3p^5 3d^3 ({}^2H) {}^3G_5^o$	5.6	70.7
195.506	1	116.8	2.5	63.2	1.4	C	Fe VII	195.485	2	$3p^6 3d^2 {}^3F_3 - 3p^5 3d^3 ({}^2H) {}^3G_4^o$	5.6	47.8
195.753	2	20.2	1.3	61.9	3.9	E, G-H						
195.993	0	312.3	3.8	66.4	0.8	D	Fe VIII	195.972	14	$3p^6 3d {}^2D_{3/2} - 3p^6 4p {}^2P_{1/2}^o$	5.7	357.0
196.074	1	80.4	2.8	60.5	2.1	B-C	Fe VII	196.046	3	$3p^6 3d^2 {}^3F_2 - 3p^5 3d^3 ({}^2H) {}^3G_3^o$	5.6	24.5
196.239	0	113.9	2.0	57.9	0.9	B-C	Fe VII	196.217	2	$3p^6 3d^2 {}^1G_4 - 3p^5 3d^3 ({}^2H) {}^1H_5^o$	5.6	38.6
196.458	1	35.8	1.4	62.5	4.0	B,L	Fe VII	196.423	3	$3p^6 3d^2 {}^3F_3 - 3p^5 3d^3 (a {}^2D) {}^3F_4^o$	5.6	4.7
196.520	4	10.1	1.2	62.5	4.0		Fe XIII	196.540	1	$3s^2 3p^2 {}^1D_2 - 3s^2 3p 3d {}^1F_3$	6.1	12.0
196.664	1	79.4	1.9	87.9	2.0	H	Fe XII	196.640	1	$3s^2 3p^3 {}^2D_{5/2}^o - 3s^2 3p^2 ({}^1D) 3d {}^2D_{5/2}$	6.1	30.7
							Fe VIII	196.650	14	$3p^6 3d {}^2D_{3/2} - 3p^5 3d^2 ({}^1S) {}^2P_{3/2}^o$	5.7	30.5
196.820	3	35.0	3.7	69.1	6.4	E-G						
196.964	6	20.5	3.5	105.8	18.2							
197.193	7	8.3	2.4	79.8	23.4							
197.387	0	193.2	2.6	71.9	0.8	D,H	Fe VIII	197.362	14	$3p^6 3d {}^2D_{5/2} - 3p^5 3d^2 ({}^1S) {}^2P_{3/2}^o$	5.7	201.0
197.871	1	188.1	12.4	76.2	2.4	E	Fe IX	197.862	16	$3s^2 3p^5 3d {}^1P_1^o - 3s^2 3p^5 4p {}^1S_0$	5.7	228.0
198.091	6	7.5	1.7	62.4	14.4							
198.256	4	12.7	2.1	57.4	8.8							
198.411	8	13.8	2.7	96.9	19.0							
198.566	2	89.6	6.8	80.0	3.9	G	S VIII	198.550	15	$2s^2 2p^5 {}^2P_{3/2}^o - 2s 2p^6 {}^2S_{1/2}$	5.8	43.5
							Fe XI	198.546	1	$3s^2 3p^4 {}^1D_2 - 3s^2 3p^3 ({}^2D) 3d {}^3P_1$	6.0	20.0
198.934	16	4.4	2.2	85.7	42.8							
199.200	12	6.3	1.5	85.0	2.7							
199.325	6	14.5	2.0	85.0	2.7	E	Mn IX	199.319	1	$3s^2 3p^5 {}^2P_{3/2}^o - 3s^2 3p^4 ({}^1D) 3d {}^2S_{1/2}$	6.0	6.8
199.613	3	34.4	2.8	85.0	2.7	E-F						
199.806	9	8.0	1.6	85.0	2.7							
200.003	3	47.7	3.4	85.0	2.7	H	Fe XIII	200.022	1	$3s^2 3p^2 {}^3P_1 - 3s^2 3p 3d {}^3D_2$	6.1	34.4

Table 4—Continued

λ	σ_λ	I	σ_I	W	σ_W	Class	Ion	λ_{ref}	Ref.	Transition	$\log T_{\text{max}}$	I_{pred}
200.161	3	31.1	2.8	85.0	2.7		Fe IX	199.986	2	$3s^2 3p^5 3d^1 D_2^o - 3s^2 3p^4 ({}^3P) 3d^2 {}^3G_3$	5.7	11.8
200.384	5	16.8	1.9	85.0	2.7							
200.686	7	17.9	2.6	85.0	2.7							
200.785	3	45.7	3.8	85.0	2.7							
201.025	6	32.2	4.3	85.0	2.7							
201.113	3	83.1	6.0	85.0	2.7	H	Fe XIII	201.128	1	$3s^2 3p^2 {}^3P_1 - 3s^2 3p 3d {}^3D_1$	6.1	37.9
201.515	8	16.3	2.7	86.9	1.6							
201.610	4	54.8	4.2	86.9	1.6	G	Fe XI	201.577	1	$3s^2 3p^4 {}^3P_2 - 3s^2 3p^3 ({}^2P) 3d {}^3P_2$	6.0	26.7
201.732	3	44.3	3.4	86.9	1.6							
201.887	2	47.7	2.9	72.9	4.3	B,H	Fe VII	201.855	3	$3p^6 3d^2 {}^3F_3 - 3p^5 3d^3 ({}^2F) {}^1G_4$	5.6	5.7
202.038	1	190.9	5.2	88.7	2.1	H	Fe XIII	202.044	1	$3s^2 3p^2 {}^3P_0 - 3s^2 3p 3d {}^3P_1$	6.1	134.0
202.344	13	9.2	3.9	55.6	23.5							
202.420	5	60.6	6.6	81.7	8.9	G	Fe VII	202.378	3	$3p^6 3d^2 {}^3F_4 - 3p^5 3d^3 ({}^2F) {}^1G_4$	5.6	1.2
202.620	4	54.7	5.1	86.9	1.6	E	S VIII	202.605	15	$2s^2 2p^5 {}^2P_{1/2}^o - 2s 2p^6 {}^2S_{1/2}$	5.8	20.1
							Fe XI	202.628	1	$3s^2 3p^4 {}^1D_2 - 3s^2 3p^3 ({}^2D) 3d {}^3P_2$	6.0	5.8
202.708	6	38.0	4.2	86.9	1.6	G	Fe XI	202.706	1	$3s^2 3p^4 {}^1D_2 - 3s^2 3p^3 ({}^2D) 3d {}^1P_1$	6.0	48.0
202.857	1	194.5	10.9	86.9	1.6	C	Cr VII	202.828	11	$3s^2 3p^6 {}^1S_0 - 3s^2 3p^5 3d {}^1P_1^o$	5.7	249.0
203.064	13	12.2	3.5	86.9	1.6							
203.138	11	18.4	3.5	86.9	1.6	I	Fe XIII	203.164	1	$3s^2 3p^2 {}^3P_1 - 3s^2 3p 3d {}^3P_0$	6.1	17.6
203.249	8	11.7	1.9	86.9	1.6							
203.634	12	15.7	3.9	100.2	5.1							
203.737	9	72.4	12.3	100.2	5.1	H	Fe XII	203.728	1	$3s^2 3p^3 {}^2D_{5/2}^o - 3s^2 3p^2 ({}^1S) 3d {}^2D_{5/2}$	6.1	28.2
203.824	4	141.1	12.7	100.2	5.1	H	Fe XIII	203.828	1	$3s^2 3p^2 {}^3P_2 - 3s^2 3p 3d {}^3D_3$	6.1	115.0
							Fe XIII	203.797	1	$3s^2 3p^2 {}^3P_2 - 3s^2 3p 3d {}^3D_2$	6.1	48.0
203.998	7	15.4	1.9	100.2	5.1							
204.173	8	25.2	3.4	100.2	5.1							
204.274	26	19.4	7.9	100.2	5.1	H-I	Fe XIII	204.263	1	$3s^2 3p^2 {}^3P_1 - 3s^2 3p 3d {}^1D_2$	6.1	14.0
204.340	32	11.6	9.1	100.2	5.1							
204.468	10	10.6	1.8	100.2	5.1							
204.722	1	211.9	11.9	72.7	1.5							
204.911	2	38.0	2.9	72.7	1.5	H-I	Fe XIII	204.945	1	$3s^2 3p^2 {}^3P_2 - 3s^2 3p 3d {}^3D_1$	6.1	11.7
205.053	1	131.2	7.5	72.7	1.5	C	Cr VIII	205.010	13	$3s^2 3p^5 {}^2P_{3/2}^o - 3s^2 3p^4 ({}^3P) 3d {}^2D_{5/2}$	5.7	48.4
205.605	7	7.8	1.5	72.7	1.5							
205.717	2	39.1	3.1	72.7	1.5		Cr VIII	205.650	13	$3s^2 3p^5 {}^2P_{1/2}^o - 3s^2 3p^4 ({}^3P) 3d {}^2D_{3/2}$	5.7	10.5
206.161	4	15.5	1.8	72.7	1.5							
206.269	4	19.7	2.2	72.7	1.5							
206.362	4	17.1	2.0	72.7	1.5		Fe XII	206.368	1	$3s^2 3p^3 {}^2D_{3/2}^o - 3s^2 3p^2 ({}^1S) 3d {}^2D_{3/2}$	6.1	6.5
206.775	2	50.5	4.0	71.4	2.7		Fe VIII	206.753	2	$3p^6 3d {}^2D_{5/2} - 3p^5 3d^2 ({}^1G) {}^2G_{7/2}$	5.6	65.3
207.031	5	19.7	2.3	71.4	2.7							
207.141	2	198.5	14.1	71.4	2.7							
207.215	4	51.5	7.8	71.4	2.7							
207.458	2	98.5	6.7	82.3	3.1							
207.743	3	89.3	8.1	72.3	6.0	B-C	Fe VII	207.712	3	$3p^6 3d^2 {}^3F_2 - 3p^5 3d^3 ({}^2F) {}^3G_3^o$	5.6	21.4
207.948	3	22.8	2.8	69.0	6.5		Ni XI	207.922	1	$3s^2 3p^6 {}^1S_0 - 3s^2 3p^5 3d {}^3P_2$	6.0	17.3
208.199	11	9.7	5.6	48.8	28.2		Fe VII	208.167	3	$3p^6 3d^2 {}^3F_3 - 3p^5 3d^3 ({}^2F) {}^3G_3^o$	5.6	3.0
208.679	2	71.4	5.6	79.2	3.9		Cr VIII	208.630	13	$3s^2 3p^5 {}^2P_{3/2}^o - 3s^2 3p^4 ({}^3P) 3d {}^2P_{3/2}$	5.7	23.2
208.846	2	99.0	7.3	71.8	2.9							
209.453	2	120.5	8.3	85.9	3.5							
209.659	6	93.9	10.1	132.2	14.2	I	Fe XIII	209.621	1	$3s^2 3p^2 {}^3P_1 - 3s^2 3p 3d {}^3P_2$	6.1	23.8
209.760	3	40.0	5.3	46.6	6.2							
209.936	2	113.9	7.8	85.9	3.5	H-I	Fe XIII	209.919	1	$3s^2 3p^2 {}^3P_2 - 3s^2 3p 3d {}^3P_1$	6.1	20.1
210.665	2	52.4	4.3	57.7	3.3							
211.306	2	124.0	8.4	131.4	5.7	H-I	Fe XIV	211.318	1	$3s^2 3p {}^2P_{1/2}^o - 3s^2 3d {}^2D_{3/2}$	6.2	136.0
211.484	4	16.3	2.4	55.0	8.2		Ni XI	211.428	1	$3s^2 3p^6 {}^1S_0 - 3s^2 3p^5 3d {}^3P_1$	6.0	6.7
							Cr VIII	211.420	13	$3s^2 3p^5 {}^2P_{1/2}^o - 3s^2 3p^4 ({}^3P) 3d {}^2P_{1/2}$	5.7	4.4
245.970	10	35.5	16.6	80.3	2.7							
246.036	2	457.7	29.6	80.3	2.7	C	Si VI	246.004	8	$2s^2 2p^5 {}^2P_{3/2} - 2s 2p^6 {}^2S_{1/2}$	5.6	543.0
246.181	3	27.3	2.2	80.3	2.7	H-I	Fe XIII	246.211	1	$3s^2 3p^2 {}^3P_1 - 3s 3p^3 {}^3S_1^o$	6.1	36.8
							Si VIII	246.124	6	$2s^2 2p^4 {}^1S_0 - 2s 2p^5 {}^1P_1^o$	5.7	5.0
247.018	2	20.1	2.1	49.5	3.7							
247.426	2	32.7	2.9	62.4	3.8	E	Al VIII	247.404	7	$2p^2 {}^3P_0 - 2s 2p^3 {}^3S_1^o$	6.0	4.6
248.489	1	105.9	6.8	70.6	2.2	A	O V	248.460	1	$2s 2p {}^1P_1^o - 2s 3s {}^1S_0$	5.6	126.0
							Al VIII	248.458	7	$2p^2 {}^3P_1 - 2s 2p^3 {}^3S_1^o$	6.0	13.8
248.668	3	34.7	3.9	61.7	6.9	A-B	Fe VII	248.641	2	$3p^6 3d^2 {}^3F_4 - 3p^5 3d^3 ({}^4F) {}^5F_4^o$	5.6	8.4
249.163	1	212.8	13.5	73.2	1.9	C,M	Si VI	249.124	8	$2s^2 2p^5 {}^2P_{1/2} - 2s 2p^6 {}^2S_{1/2}$	5.6	257.0

Table 4—Continued

λ	σ_λ	I	σ_I	W	σ_W	Class	Ion	λ_{ref}	Ref.	Transition	$\log T_{\text{max}}$	I_{pred}
249.329	3	70.4	5.4	87.2	6.1	H-I	Fe VII	249.302	2	$3p^6 3d^2 {}^3F_4 - 3p^5 3d^3 ({}^4F) {}^5F_5^o$	5.6	14.2
250.155	2	24.7	2.4	60.1	4.1	E	Al VIII	250.139	7	$2p^2 {}^3P_2 - 2s2p^3 {}^3S_1^o$	6.0	23.2
250.514	3	5.3	1.0	35.7	5.9		Si VIII	250.465	5	$2s^2 2p^3 {}^2P_{1/2}^o - 2s2p^4 {}^2S_{1/2}$	6.0	3.4
250.823	5	6.9	1.1	61.1	9.4		Si VIII	250.807	5	$2s^2 2p^3 {}^2P_{3/2}^o - 2s2p^4 {}^2S_{1/2}$	6.0	5.2
251.932	3	44.1	3.0	113.8	5.3	H-I	Fe XIII	251.956	1	$3s^2 3p^2 {}^3P_2 - 3s3p^3 {}^3S_1^o$	6.1	70.9
252.918	4	12.9	1.7	88.8	10.0							
253.555	3	19.0	2.7	55.2	7.8	A-D	Fe VII	253.528	2	$3p^6 3d^2 {}^3F_3 - 3p^5 3d^3 ({}^4F) {}^5D_3^o$	5.6	5.2
253.771	4	19.9	1.9	109.1	9.1	H	Si X	253.788	1	$2s^2 2p^2 P_{1/2}^o - 2s2p^2 {}^2P_{3/2}$	6.1	26.1
253.981	1	285.9	7.1	70.1	1.6	C-D	Fe VIII	253.953	1	$3p^6 3d {}^2D_{5/2} - 3p^5 3d^2 ({}^3F) {}^4D_{7/2}$	5.6	223.0
254.085	3	49.4	4.6	68.7	6.4	B	Fe VII	254.057	2	$3p^6 3d {}^2F_4 - 3p^5 3d^3 ({}^4F) {}^5D_4^o$	5.6	11.4
254.223	2	22.0	2.1	60.9	4.2							
254.590	4	11.9	1.5	62.1	7.5							
254.706	2	36.7	3.1	71.6	4.2							
255.132	1	112.9	4.5	66.1	2.1	C-D	Fe VIII	255.103	1	$3p^6 3d {}^2D_{3/2} - 3p^5 3d^2 ({}^3F) {}^4D_{3/2}$	5.6	129.0
255.373	1	193.9	5.5	72.2	1.6	C-D	Fe VIII	255.344	1	$3p^6 3d {}^2D_{5/2} - 3p^5 3d^2 ({}^3F) {}^4D_{5/2}$	5.6	127.0
255.707	2	56.4	3.3	66.1	3.4	C	Fe VIII	255.678	1	$3p^6 3d {}^2D_{3/2} - 3p^5 3d^2 ({}^3F) {}^4D_{1/2}$	5.6	89.5
256.045	5	8.6	1.4	78.1	13.0							
256.345	1	608.0	27.9	95.9	1.5	A	He II	256.317	1	$1s {}^2S_{1/2} - 3p {}^2P_{3/2}^o$	4.9	1270.0
							He II	256.318	1	$1s {}^2S_{1/2} - 3p {}^2P_{1/2}^o$	4.9	632.0
							Si X	256.366	1	$2s^2 2p {}^2P_{1/2}^o - 2s2p^2 {}^2P_{1/2}$	6.1	56.6
256.466	4	65.4	6.7	95.9	1.5	G	Fe X	256.398	1	$3s^2 3p^5 {}^2P_{3/2}^o - 3s^2 3p^4 ({}^3P) 3d {}^4D_{3/2}$	6.0	22.9
							Fe XII	256.410	1	$3s^2 3p^3 {}^2D_{5/2}^o - 3s^2 3p^2 ({}^3P) 3d {}^4F_{7/2}$	6.1	14.5
							Fe XIII	256.422	1	$3s^2 3p^2 {}^1D_2 - 3s3p^3 {}^1P_1^o$	6.1	13.6
256.922	3	35.1	2.6	95.9	1.5							
257.182	10	17.0	3.8	83.9	1.4		S X	257.147	1	$2s^2 2p^3 {}^4S_{3/2} - 2s2p^4 {}^4P_{1/2}$	6.1	7.9
257.275	1	396.4	7.3	83.9	1.4	F	Fe X	257.259	1	$3s^2 3p^5 {}^2P_{3/2}^o - 3s^2 3p^4 ({}^3P) 3d {}^4D_{5/2}$	6.0	55.6
							Fe X	257.263	1	$3s^2 3p^5 {}^2P_{3/2}^o - 3s^2 3p^4 ({}^3P) 3d {}^4D_{7/2}$	6.0	126.0
257.420	6	17.7	2.0	83.9	1.4							
257.545	3	41.8	2.4	83.9	1.4	G-H	Fe XI	257.547	1	$3s^2 3p^4 {}^3P_2 - 3s^2 3p^3 ({}^4S) 3d {}^5D_3^o$	6.0	12.3
257.768	5	17.4	2.0	83.9	1.4	G-H	Fe XI	257.772	1	$3s^2 3p^4 {}^3P_2 - 3s^2 3p^3 ({}^4S) 3d {}^5D_2^o$	6.0	6.3
258.089	3	21.2	2.1	85.4	7.2		Si IX	258.082	7	$2s^2 2p^2 {}^1D_2 - 2s2p^3 {}^1D_2^o$	6.0	20.3
258.369	2	109.4	6.7	95.5	3.0	G-H	Si X	258.371	1	$2s^2 2p {}^2P_{3/2}^o - 2s2p^2 {}^2P_{3/2}$	6.1	136.0
258.636	4	5.1	1.0	51.6	10.0		Cr VII	258.655	11	$3s^2 3p^6 {}^1S_0 - 3s^2 3p^5 3d {}^3D_2^o$	5.7	1.5
259.226	2	13.0	1.6	55.4	4.9	A-D	Cr VII	259.181	11	$3s^2 3p^6 {}^1S_0 - 3s^2 3p^5 3d {}^3D_1^o$	5.7	3.5
							Al VII	259.196	5	$2s^2 2p^3 {}^2P_{3/2}^o - 2s2p^4 {}^2P_{1/2}$	5.7	2.3
259.515	4	27.7	2.2	127.9	8.2	H	S X	259.497	1	$2s^2 2p^3 {}^4S_{3/2}^o - 2s2p^4 {}^4P_{3/2}$	6.1	15.3
259.985	2	27.9	2.4	72.6	4.2							
260.141	3	4.8	1.0	40.2	6.9							
260.295	4	16.7	1.8	111.2	10.1		O IV	260.389	1	$2s2p^2 {}^2D_{5/2} - 2s2p ({}^3P) 3d {}^2F_{7/2}^o$	5.2	16.9
260.707	3	19.8	1.9	67.7	6.1	B-C	Fe VII	260.678	2	$3p^6 3d^2 {}^3P_2 - 3p^5 3d^3 ({}^4F) {}^5F_3^o$	5.6	5.3
261.053	2	47.9	3.4	91.0	4.0	H	Si X	261.044	1	$2s^2 2p {}^2P_{3/2}^o - 2s2p^2 {}^2P_{1/2}$	6.1	50.6
261.242	4	4.6	0.9	50.6	10.0		Al VII	261.209	1	$2s^2 2p^3 {}^2P_{3/2}^o - 2s2p^4 {}^2P_{3/2}$	5.7	4.8
261.354	6	5.0	1.1	70.1	14.9		Cr VII	261.314	11	$3s^2 3p^6 {}^1S_0 - 3s^2 3p^5 3d {}^1D_2^o$	5.7	0.6
261.728	6	7.5	1.3	94.8	15.0							
262.303	6	4.0	0.9	58.9	13.3							
262.696	17	2.1	1.0	87.0	39.3							
262.988	4	8.4	1.2	70.8	9.3	L-M	Fe XVI	262.976	1	$3p {}^2P_{3/2}^o - 3d {}^2D_{5/2}$	6.4	5.9
263.200	4	10.8	1.4	76.0	8.6		Mn VIII	263.163	12	$3s^2 3p^6 {}^1S_0 - 3s^2 3p^5 3d {}^3P_2^o$	5.7	4.0
264.239	3	21.9	2.1	97.6	7.4	H	S X	264.231	1	$2s^2 2p^3 {}^4S_{3/2}^o - 2s2p^4 {}^4P_{5/2}$	6.1	22.3
264.375	7	3.2	1.0	54.9	16.7							
264.630	20	5.2	2.0	101.9	39.2							
264.780	3	68.4	4.4	115.1	6.1	I	Fe XIV	264.790	1	$3s^2 3p {}^2P_{3/2}^o - 3s3p^2 {}^2P_{3/2}$	6.2	68.2
265.738	3	11.6	1.3	64.8	7.2	B,L	Fe VII	265.697	3	$3p^6 3d^2 {}^1S_0 - 3p^6 3d4p {}^1P_1^o$	5.6	4.9
266.106	5	14.7	1.6	87.4	3.6							
266.208	5	13.1	1.5	87.4	3.6							
266.531	8	9.1	1.5	87.4	3.6							
266.623	5	15.1	1.8	87.4	3.6							
267.245	6	13.7	2.8	70.4	6.8	B	Fe VII	267.231	2	$3p^6 3d^2 {}^3P_2 - 3p^5 3d^3 ({}^4F) {}^5D_3^o$	5.6	1.4
							Fe VII	267.250	2	$3p^6 3d^2 {}^3P_2 - 3p^5 3d^3 ({}^4F) {}^5D_1^o$	5.6	1.7
267.303	4	19.8	2.4	70.4	6.8	B	Fe VII	267.274	2	$3p^6 3d^2 {}^3P_2 - 3p^5 3d^3 ({}^4F) {}^5D_2^o$	5.6	4.3
268.043	7	6.0	1.0	87.4	3.6							
268.228	8	5.1	1.0	87.4	3.6							
269.020	1	249.7	15.0	83.6	2.0	C	Mg VI	268.991	5	$2s^2 2p^3 {}^2D_{3/2}^o - 2s2p^4 {}^2P_{1/2}$	5.7	213.0
269.561	6	8.4	1.2	83.6	2.0							
269.817	14	2.8	1.0	83.6	2.0							
270.426	1	522.2	30.7	83.9	2.2	C	Mg VI	270.390	5	$2s^2 2p^3 {}^2D_{5/2}^o - 2s2p^4 {}^2P_{3/2}$	5.7	370.0
							Mg VI	270.400	5	$2s^2 2p^3 {}^2D_{3/2}^o - 2s2p^4 {}^2P_{3/2}$	5.7	49.5

Table 4—Continued

λ	σ_λ	I	σ_I	W	σ_W	Class	Ion	λ_{ref}	Ref.	Transition	$\log T_{\text{max}}$	I_{pred}
270.539	8	17.4	3.5	67.2	13.5	I	Fe xiv	270.522	1	$3s^2 3p^2 P_{3/2}^o - 3s 3p^2 P_{1/2}$	6.2	38.9
271.068	6	17.6	1.9	124.1	13.1	A	O v	270.978	1	$2p^2 \ ^3P_2 - 2s 3p \ ^3P_2^o$	5.6	9.3
							O v	271.035	1	$2p^2 \ ^3P_2 - 2s 3p \ ^3P_1^o$	5.6	1.6
271.729	2	24.7	1.7	79.8	5.1	B	Fe vii	271.699	2	$3p^6 3d^2 \ ^3P_2 - 3p^5 3d^3 \ (^4P) \ ^5S_2^o$	5.6	5.3
271.990	3	51.2	3.8	113.4	7.3	H	Si x	272.006	1	$2s^2 2p^2 P_{1/2}^o - 2s 2p^2 \ ^2S_{1/2}$	6.1	38.1
272.153	7	16.2	2.5	99.7	15.6							
272.339	6	11.2	2.0	94.6	16.8							
272.685	1	235.7	12.6	84.6	1.6	D	Si vii	272.647	6	$2s^2 2p^4 \ ^3P_2 - 2s 2p^5 \ ^3P_1^o$	5.7	214.0
274.119	7	15.4	2.8	84.6	1.6							
274.218	2	217.2	11.4	84.6	1.6	C,I	Si vii	274.180	6	$2s^2 2p^4 \ ^3P_1 - 2s 2p^5 \ ^3P_0^o$	5.7	142.0
							Fe xiv	274.204	1	$3s^2 3p^2 P_{1/2}^o - 3s 3p^2 \ ^2S_{1/2}$	6.2	74.9
275.394	1	699.4	37.9	90.5	1.5	C	Si vii	275.361	6	$2s^2 2p^4 \ ^3P_{1/2} - 2s 2p^5 \ ^3P_2^o$	5.7	706.0
275.715	1	133.3	3.1	78.0	1.4	C	Si vii	275.675	6	$2s^2 2p^4 \ ^3P_1 - 2s 2p^5 \ ^3P_1^o$	5.7	123.0
276.174	1	142.9	2.8	79.2	1.0	C	Mg vii	276.138	7	$2s^2 2p^2 \ ^3P_0 - 2s 2p^3 \ ^3S_1^o$	5.7	100.0
276.625	1	225.0	4.4	76.5	1.1	B	Mg v	276.579	6	$2s^2 2p^4 \ ^1D_2 - 2s 2p^5 \ ^1P_1^o$	5.6	245.0
276.873	2	140.9	6.4	100.2	2.4		Si viii	276.850	5	$2s^2 2p^3 \ ^2D_{5/2}^o - 2s 2p^4 \ ^2D_{3/2}$	6.0	85.2
276.881	2	8.0	0.3	100.2	2.4		Si viii	276.865	5	$2s^2 2p^3 \ ^2D_{3/2}^o - 2s 2p^4 \ ^2D_{5/2}$	6.0	4.7
276.891	1	174.7	4.1	78.0	1.4		Si vii	276.850	6	$2s^2 2p^4 \ ^3P_0 - 2s 2p^5 \ ^3P_1^o$	5.7	160.0
277.023	1	427.4	8.2	79.2	1.0		Mg vii	276.993	7	$2s^2 2p^2 \ ^3P_1 - 2s 2p^3 \ ^3S_1^o$	5.7	299.0
277.066	2	12.3	0.6	100.2	2.4		Si viii	277.042	5	$2s^2 2p^3 \ ^2D_{5/2}^o - 2s 2p^4 \ ^2D_{3/2}$	6.0	7.4
277.074	2	201.0	8.7	100.2	2.4		Si viii	277.057	5	$2s^2 2p^3 \ ^2D_{5/2}^o - 2s 2p^4 \ ^2D_{5/2}$	6.0	119.0
277.255	3	31.7	2.3	97.9	7.0	H	Si x	277.278	1	$2s^2 2p^2 P_{3/2}^o - 2s 2p^2 \ ^2S_{1/2}$	6.1	31.2
277.625	5	11.6	1.6	86.5	11.3							
278.426	1	750.2	17.5	87.3	1.7	D	Mg vii	278.393	7	$2s^2 2p^2 \ ^3P_2 - 2s 2p^3 \ ^3S_1^o$	5.7	502.0
278.484	2	236.1	26.4	87.3	1.7	D	Si vii	278.449	6	$2s^2 2p^4 \ ^3P_1 - 2s 2p^5 \ ^3P_2^o$	5.7	226.0
278.731	3	29.4	2.8	84.4	5.8	B	Al v	278.694	10	$2s^2 2p^5 \ ^2P_{3/2}^o - 2s 2p^6 \ ^2S_{1/2}$	5.6	20.9
							Ni xi	278.684	17	$3s^2 3p^5 3d \ ^3F_4 - 3s 3p^6 3d \ ^3D_3$	5.9	3.0
278.898	5	6.4	1.2	59.6	10.9							
279.670	3	14.7	1.8	72.7	7.5	A	O iv	279.631	1	$2s^2 2p^2 P_{1/2}^o - 2s^2 3s \ ^2S_{1/2}$	5.2	22.0
279.973	2	43.1	3.4	73.0	3.7	A	O iv	279.933	1	$2s^2 2p^2 P_{3/2}^o - 2s^2 3s \ ^2S_{1/2}$	5.2	44.1
280.759	1	220.0	12.9	83.4	1.9	D	Mg vii	280.722	7	$2s^2 2p^2 \ ^1D_2 - 2s 2p^3 \ ^1P_1^o$	5.7	176.0
281.438	3	10.5	1.4	54.7	6.2	A-D,I	Al v	281.394	10	$2s^2 2p^5 \ ^2P_{1/2}^o - 2s 2p^6 \ ^2S_{1/2}$	5.6	10.0
282.443	4	14.2	1.7	79.3	7.7		Al ix	282.421	1	$2s^2 2p^2 P_{1/2}^o - 2s 2p^2 \ ^2P_{1/2}$	6.0	10.0
283.981	9	16.3	3.5	84.5	3.0							
284.063	6	50.3	4.8	84.5	3.0	G-H	Al ix	284.025	1	$2s^2 2p^2 P_{3/2}^o - 2s 2p^2 \ ^2P_{3/2}$	6.0	27.4
284.173	2	161.7	10.2	84.5	3.0	L	Fe xv	284.163	1	$3s^2 \ ^1S_0 - 3s 3p \ ^1P_1^o$	6.3	281.0
286.375	5	8.4	1.3	69.2	9.2		Al ix	286.376	1	$2s^2 2p^2 P_{3/2}^o - 2s 2p^2 \ ^2P_{1/2}$	6.0	7.9
289.727	4	38.0	5.3	74.1	10.4	A-D	Fe vii	289.678	2	$3p^6 3d^2 \ ^3F_2 - 3p^6 3d 4s \ ^3D_2$	5.6	12.8
289.884	3	36.6	4.8	57.2	7.5	A-D	Fe vii	289.831	2	$3p^6 3d^2 \ ^3F_3 - 3p^6 3d 4s \ ^3D_3$	5.6	12.6
290.345	3	69.6	6.2	72.2	6.2	B	Fe vii	290.307	2	$3p^6 3d^2 \ ^3F_2 - 3p^6 3d 4s \ ^3D_1$	5.6	17.6
290.704	10	34.1	7.5	80.1	4.7		Si ix	290.687	7	$2s^2 2p^2 \ ^3P_0 - 2s 2p^3 \ ^3P_1^o$	6.0	34.8
290.791	2	178.8	10.4	80.1	4.7	B	Fe vii	290.717	2	$3p^6 3d^2 \ ^3F_3 - 3p^6 3d 4s \ ^3D_2$	5.6	21.1
							Fe vii	290.756	2	$3p^6 3d^2 \ ^3F_4 - 3p^6 3d 4s \ ^3D_3$	5.6	45.2

Table 5: Reference wavelength sources.

Index	Reference
1	CHIANTI 6.0 Dere et al. (2009)
2	Young & Landi (2009)
3	Ekberg (1981)
4	Edlén (1934)
5	Edlén (1984)
6	Edlén (1983)
7	Edlén (1985)
8	Artru & Brillet (1977)
9	Edlén (1979)
10	Artru & Brillet (1974)
11	Ekberg (1976)
12	Smitt & Svensson (1983)
13	Fawcett & Gabriel (1966)
14	Ramonas & Ryabtsev (1980)
15	Robinson (1937)
16	Young (2009)
17	Present work

Table 6: Emission line velocities.

Index	T_{eff}	λ	v_{ref}	v_{NIST}	σ_v
O IV	5.21	279.670	41.8	41.8	3.2
		279.973	42.8	42.8	2.1
O V	5.49	192.931	42.0	38.9	1.6
		248.489	35.0	36.2	1.2
Al V	5.56	278.731	39.8	39.8	3.2
		281.438	46.9	46.9	3.2
Mg V	5.60	276.625	49.9	46.6	0.5
O VI	5.64	183.951	19.6	22.8	3.3
		184.141	35.8	39.1	3.3
Si VI	5.65	246.036	39.0	39.0	2.4
		249.163	46.9	46.9	1.2
Mg VI	5.68	269.020	32.3	34.5	1.1
		270.426	39.9	37.7	1.1
Cr VII	5.69	202.857	42.9	42.9	1.5
Fe VIII	5.70	185.232	30.7	30.7	0.0
		186.627	45.0	45.0	1.6
Si VII	5.74	272.685	41.8	50.6	1.1
		274.218	41.5	47.0	2.2
		275.394	35.9	44.7	1.1
		275.715	43.5	52.2	0.8
		278.484	37.7	44.2	2.2
Mn VIII	5.74	185.467	19.4	19.4	3.2
Al VII	5.76	261.242	39.0	26.4	4.6
		259.226	34.7	22.0	2.3
Mg VII	5.76	276.174	39.1	22.8	0.5
		278.426	35.5	25.8	1.1
		280.759	39.5	23.5	1.1
Cr VIII	5.88	205.053	62.9	62.9	1.5
Si VIII	5.89	250.514	58.7	76.6	3.6
		250.823	19.1	39.4	6.0
		276.873	24.9	37.9	2.2
		277.074	18.4	20.6	2.2
Al VIII	5.92	250.155	19.2	19.2	2.4